

**Sensitivity of Polarization to Grain Shape: I. Convex Shapes**B. T. DRAINE<sup>1</sup><sup>1</sup>*Dept. of Astrophysical Sciences, Princeton University, Princeton, NJ 08544, USA*

## ABSTRACT

Aligned interstellar grains produce polarized extinction (observed at wavelengths from the far-ultraviolet to the mid-infrared), and polarized thermal emission (observed at far-infrared and submm wavelengths). The grains must be quite nonspherical, but the actual shapes are unknown. The *relative* efficacy for aligned grains to produce polarization at optical vs. infrared wavelengths depends on particle shape. The discrete dipole approximation is used to calculate polarization cross sections for 20 different convex shapes, for wavelengths from  $0.1\mu\text{m}$  to  $100\mu\text{m}$ , and grain sizes  $a_{\text{eff}}$  from  $0.05\mu\text{m}$  to  $0.3\mu\text{m}$ . Spheroids, cylinders, square prisms, and triaxial ellipsoids are considered. Minimum aspect ratios required by the observed starlight polarization are determined. Some shapes can also be ruled out because they provide too little or too much polarization at far-infrared and sub-mm wavelengths. The ratio of  $10\mu\text{m}$  polarization to integrated optical polarization is almost independent of grain shape, varying by only  $\pm 8\%$  among the viable convex shapes; thus, at least for convex grains, uncertainties in grain shape cannot account for the discrepancy between predicted and observed  $10\mu\text{m}$  polarization toward Cyg OB2-12.

*Keywords:* interstellar dust (836), radiative transfer (1335)

## 1. INTRODUCTION

Since the discovery of starlight polarization over 70 years ago (Hiltner 1949; Hall 1949), polarization has become a valuable tool for studying both the physical properties of interstellar dust and the structure of the Galactic magnetic field. Initially unpolarized starlight propagating through the interstellar medium (ISM) becomes linearly polarized as a result of polarization-dependent extinction (linear dichroism) by the aligned dust grains in the ISM. While the physics of dust grain alignment is not yet fully understood, early investigations (Davis & Greenstein 1951) showed how spinning dust grains could become aligned with shortest axes tending to be parallel to the local magnetic field  $\mathbf{B}_0$ . Subsequent studies identified a number of important physical processes that were initially overlooked (see the review by Andersson et al. 2015), but it remains clear that in the diffuse ISM the magnetic field establishes the direction of grain alignment, with dust grains tending to align with their short axes parallel to  $\mathbf{B}_0$ .

The aligned grains responsible for starlight polarization also produce polarized thermal emission at far-infrared and submillimeter wavelengths, now mapped over the full sky (Planck Collaboration et al. 2016). The fractional polarization of the thermal emission measured by Planck (Planck Collaboration et al. 2020) and Blastpol (Ashton et al. 2018) is nearly independent of wavelength from  $250\mu\text{m}$  to 3 mm (see Figure 13 in Hensley & Draine 2021), motivating the “astrodust” model (Hensley &

Draine 2023), where the extinction and emission are dominated by a single composite grain material, incorporating both silicate and nonsilicate constituents. In the astrodust model, a single grain type accounts for the observed polarization across the entire wavelength range, from far-UV (FUV) to far-infrared (FIR).

The present paper is a study of the optics of the small particles responsible for starlight polarization and polarized FIR emission. For reasons of analytic and computational convenience, spheroids – the simplest nonspherical shape – are often assumed when modeling polarization by interstellar grains (e.g. Kim & Martin 1995; Draine & Fraisse 2009; Siebenmorgen et al. 2014; Guillet et al. 2018; Draine & Hensley 2021a; Hensley & Draine 2023). However, interstellar grains are not ideal spheroids. Here we use the discrete dipole approximation (DDA) to calculate accurate extinction and polarization cross sections for a variety of grain shapes, to compare with spheroids, and to find shapes consistent with observational constraints.

Starlight polarization in the ISM is due to aligned nonspherical grains with sizes comparable to the vacuum wavelength  $\lambda$ ; scattering is important. At mid-IR and submm wavelengths, however, the grain optics enters a different regime: the grains are small compared to  $\lambda$ , absorption dominates, and scattering is negligible. We study the grain optics from the FUV ( $0.1\mu\text{m}$ ) to the FIR ( $100\mu\text{m}$ ). The following questions are investigated:

1. What shapes are consistent with the observed *strength* of starlight polarization at optical wavelengths?
2. What shapes are compatible with the observed *width* of the starlight polarization as a function of  $\lambda$ ?
3. For a given strength of starlight polarization, how does the fractional polarization of the submm emission depend on grain shape? Do small-scale features such as sharp edges or corners affect the polarizing ability at optical wavelengths (grain size  $\sim\lambda$ ) relative to very long wavelengths (size  $\ll\lambda$ )?
4. Can the extinction and polarization properties of nonspheroidal shapes be adequately approximated by spheroids with suitable axial ratio?
5. For a given strength of starlight polarization, how does  $10\mu\text{m}$  polarization depend on the grain shape? A recent measurement by Telesco et al. (2022) of starlight polarization at  $10\mu\text{m}$  found weaker polarization than had been predicted by grain models that assumed spheroidal grains. Can nonspheroidal shapes explain this?

The present paper examines a number of convex shapes. Included are spheroidal and ellipsoidal grains with smoothly rounded surfaces, and also shapes (cylinders and square prisms) with sharp edges and corners. We consider both elongated and flattened shapes. Some of the studied shapes are found to be compatible with observations of interstellar polarization, but others are not.

1. For spheroids, cylinders and square prisms we determine the minimum aspect ratios that are compatible with the observed strength of starlight polarization.
2. Some of the considered shapes could reproduce the integrated strength of starlight polarization, but are ruled out because the resulting polarization profile would be too broad.
3. Some of the considered geometries (e.g., elongated cylinders) would overproduce the observed fractional polarization at FIR wavelengths if required to reproduce the observed starlight polarization, while other geometries (e.g., the flattened cylinder) would fall short of the observed FIR polarization.

4. We show that grain shape does have systematic effects on the relative amounts of polarization at optical and infrared wavelengths; however, the effects are relatively modest, so that spheroids remain a useful approximation.
5. We find that the predicted ratio of  $10\mu\text{m}$  polarization to optical starlight polarization is only weakly dependent on grain shape.

The target shapes considered are presented in section 2. The dielectric functions used here are discussed in section 3. The treatment of absorption and scattering by both axisymmetric and non-axisymmetric grains is outlined in section 4. The accuracy of the DDA is examined in section 5. Extinction and polarization cross sections are presented in section 6. Observational constraints provided by the starlight polarization are summarized in section 7. The characteristic wavelength  $\lambda_p$  and profile width  $\sigma_p$  for starlight polarization are evaluated in section 8, and the polarization efficiency integral  $\Phi$  is calculated for the considered shapes in section 9.

The results are discussed in section 10, and summarized in section 11. Certain technical matters pertaining to application of the DDA are discussed in the Appendices.

## 2. TARGET GEOMETRY

Draine & Hensley (2021a) found that prolate spheroids with 2:1:1 axial ratios, and oblate spheroids with 5:7:7 axial ratios, were allowed by observations of starlight polarization, whereas spheroids with less extreme axial ratios could not provide sufficient polarization. The present study includes these two spheroidal shapes, plus other shapes with various degrees of elongation or flattening.

The target size is specified by the radius of an equal-volume sphere:  $a_{\text{eff}} \equiv (3V/4\pi)^{1/3}$ , where  $V$  is the solid volume. Optical cross sections depend on the dielectric function, grain shape, and the ratio  $a_{\text{eff}}/\lambda$ .

Polarization arises from asymmetry in the grain shape. We can characterize the asymmetry of a given shape by the ratio of a long dimension to a short dimension. We can also characterize the grain asymmetry using the moment of inertia tensor, assuming the solid material in the grain to have a single density  $\rho$ . Define

$$\alpha_j \equiv \frac{I_j}{0.4\rho V a_{\text{eff}}^2} \quad , \quad (1)$$

where  $I_1 \geq I_2 \geq I_3$  are the eigenvalues of the moment of inertia tensor. A sphere has  $\alpha_1 = \alpha_2 = \alpha_3 = 1$ ; all other shapes have  $\alpha_1 > 1$ , and  $\alpha_1 + \alpha_2 + \alpha_3 > 3$ .

One measure of the asymmetry of the grain is provided by the ‘‘asymmetry’’ parameter

$$\mathcal{A} \equiv \frac{\alpha_1}{(\alpha_2\alpha_3)^{1/2}} \geq 1 \quad . \quad (2)$$

A sphere or a cube has  $\mathcal{A} = 1$ , but  $\mathcal{A}$  becomes large for very flattened or elongated shapes. The twenty shapes in this study have  $1.19 < \mathcal{A} < 2.16$ .

Flattening or elongation of the shape can be characterized by the ‘‘stretch’’ parameter

$$\mathcal{S} \equiv \frac{\alpha_2}{(\alpha_1\alpha_3)^{1/2}} \quad , \quad (3)$$

with  $\frac{1}{\sqrt{2}} < \mathcal{S} < 1$  for flattened shapes, and  $\mathcal{S} > 1$  for elongated shapes. Extreme flattening corresponds to  $\mathcal{S} \rightarrow \frac{1}{\sqrt{2}}$ , and extreme elongation to  $\mathcal{S} \gg 1$ . The shapes in this study have  $0.79 < \mathcal{S} < 2.16$ .

Four shape classes are considered:

1. **Spheroids:** Axial length  $L$ , diameter  $D$ ,  $a_{\text{eff}} = (D^2L/8)^{1/3}$ . We consider two flattened (oblate) spheroids ( $D/L = 1.4, 2.0$ ) and two elongated (prolate) spheroids ( $L/D = 1.5, 2.0$ ).

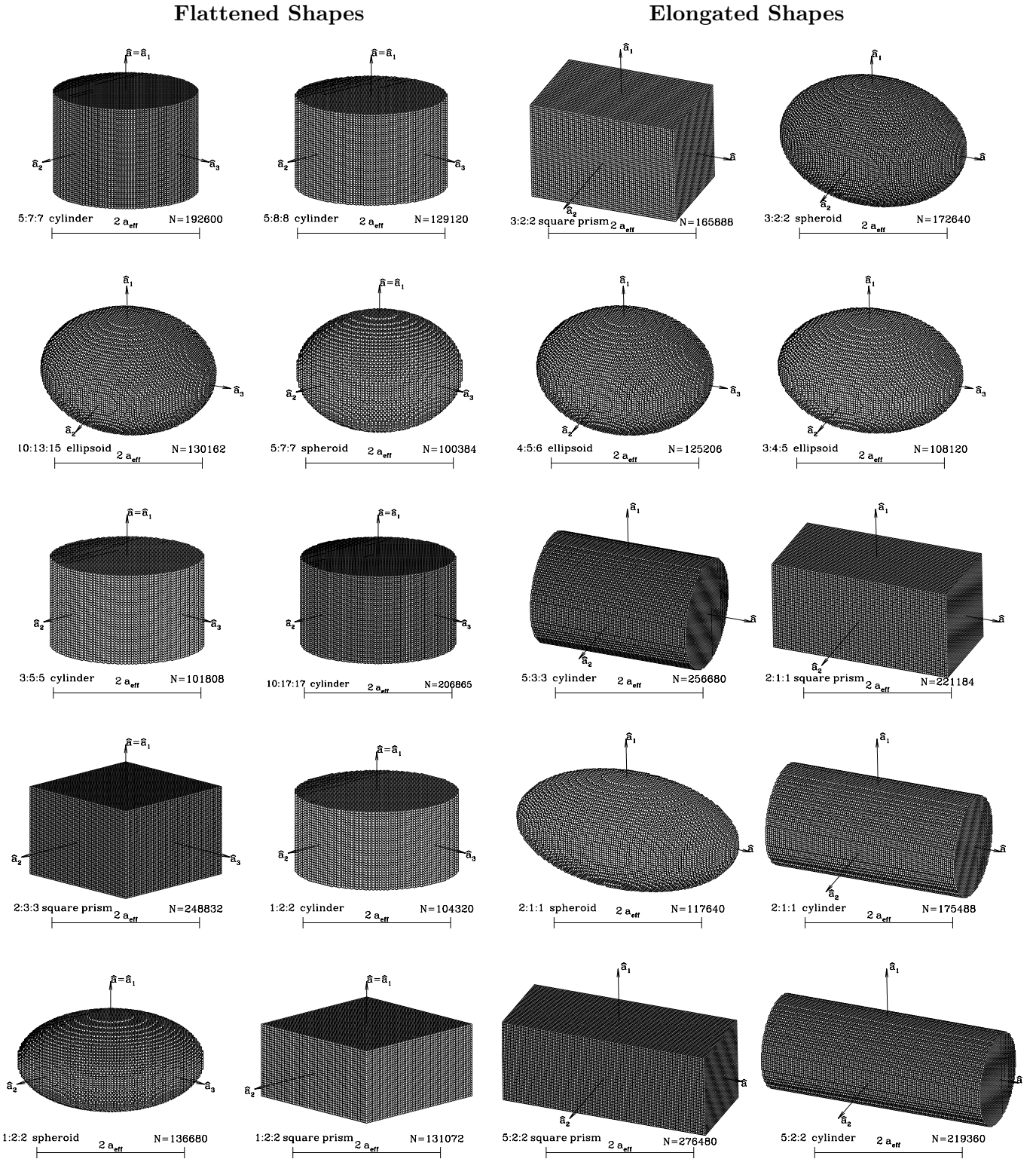


**Figure 1.** 20 convex shapes in this study. Scale bars show  $2a_{\text{eff}}$   $\hat{\mathbf{a}}_1$  is the principal axis of largest moment of inertia; grains are assumed to spin around this axis. For grains with rotational symmetry,  $\hat{\mathbf{a}}$  is the symmetry axis: 12 of the examples are axisymmetric; the 5 square prisms have 4-fold rotational symmetry.

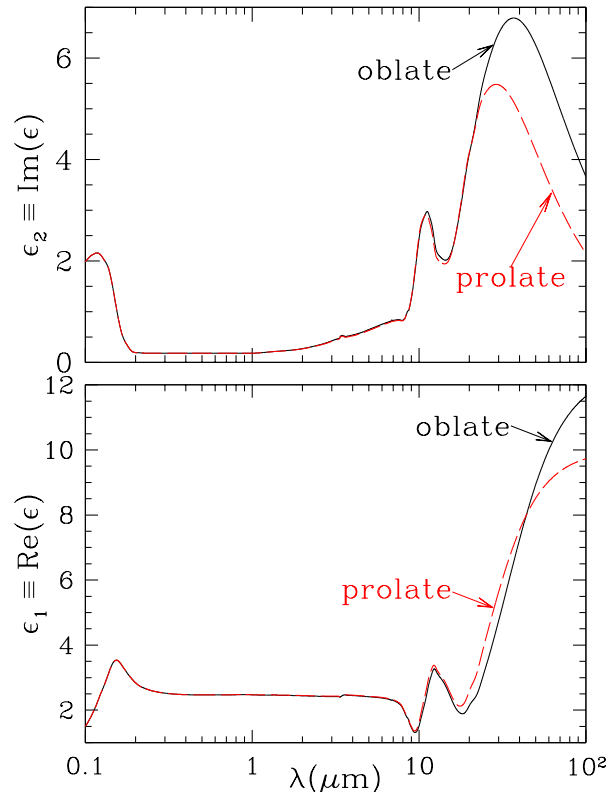


**Figure 2.** Black curves:  $\epsilon(\lambda)$  used for flattened shapes. Red curves:  $\epsilon(\lambda)$  used for elongated shapes. See text.

2. **Cylinders:** Axial length  $L$ , diameter  $D$ ,  $a_{\text{eff}} = (3D^2L/16)^{1/3}$ . Elongated ( $\mathcal{S} > 1$ ) cylinders have  $L/D > \sqrt{3/4} = 0.866$ ; flattened ( $\mathcal{S} < 1$ ) cylinders have  $L/D < 0.866$ . We consider five flattened cylinders ( $D/L = 1.4, 1.6, 1.67, 1.7, 2$ ) and three elongated cylinders ( $L/D = 1.5, 2.0, 2.5$ ).
3. **Square Prisms:** Axial length  $L$ , width  $W$ ,  $a_{\text{eff}} = (3W^2L/4\pi)^{1/3}$ , and fourfold rotational symmetry around the axis  $\hat{\mathbf{a}}$ . We consider two flattened shapes ( $W/L = 1.5, 2.0$ ) and three elongated shapes ( $L/W = 1.5, 2.0, 2.5$ ).
4. **Triaxial Ellipsoids:** Axial lengths  $L_1 < L_2 < L_3$ ,  $a_{\text{eff}} = (L_1L_2L_3/8)^{1/3}$ . We consider three examples:  $L_1:L_2:L_3 = 4:5:6$ ,  $10:13:15$ , and  $3:4:5$ . These all have  $\mathcal{S} \approx 1$ , and thus are neither very flattened nor very elongated.

Twenty convex shapes, shown in Figure 1, have been studied. Ten are “flattened” ( $\mathcal{S} < 1$ ), and ten are “elongated” ( $\mathcal{S} > 1$ ).  $\alpha_j$ ,  $\mathcal{A}$ , and  $\mathcal{S}$  for the shapes in this study can be found in Table 1.

### 3. DIELECTRIC FUNCTION

The complex dielectric function  $\epsilon(\lambda) = \epsilon_1 + i\epsilon_2$  characterizes the response of a substance to a local electric field oscillating at frequency  $c/\lambda$ . The dielectric function of interstellar grain material remains uncertain. [Draine & Hensley \(2021a\)](#) (hereafter DH21a) obtained dielectric functions for a hypothetical material (“astrodust”) intended to represent the bulk of the interstellar grain material. The derived dielectric function depended on the assumed grain shape and porosity; DH21a considered several different spheroidal shapes and porosities. The mid- and far-infrared dielectric function was “derived” by requiring that  $\epsilon(\lambda)$  obey the Kramers-Kronig relations and that the dust model reproduce the observed infrared and submm opacity of the diffuse ISM.

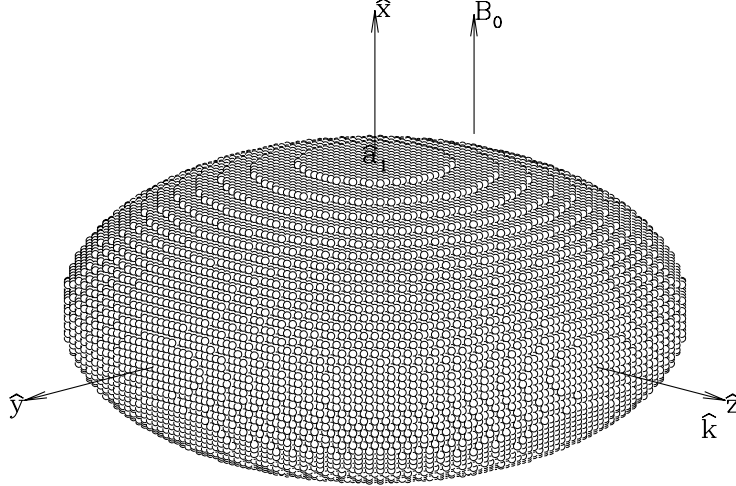


**Figure 3.** Perfect spinning alignment (PSA) geometry. The grain is spinning around principal axis  $\hat{\mathbf{a}}_1$ , with  $\hat{\mathbf{a}}_1 \parallel \mathbf{B}_0$ , the local magnetic field. Polarization is maximum for radiation propagating with  $\hat{\mathbf{k}} \perp \mathbf{B}_0$ .

Figure 2 shows the effective dielectric function  $\epsilon(\lambda)$  derived by DH21a if astro dust is assumed to have microporosity  $\mathcal{P}_{\text{micro}} = 0.2$ , and the grains are taken to be either 5:7:7 oblate spheroids or 2:1:1 prolate spheroids. The two dielectric functions are very similar for  $\lambda \lesssim 15\mu\text{m}$  (see Figure 2) but differ at longer wavelengths. The material is strongly absorptive ( $\epsilon_2 \gtrsim 0.5$ ) in the vacuum UV and also in the mid-IR and FIR. The real part  $\epsilon_1$  is large in the FIR.

We use the “oblate” dielectric function in Figure 2 for the “flattened” shapes, and the “prolate” dielectric function from Figure 2 for the “elongated” shapes.

#### 4. SCATTERING AND ABSORPTION

The dimensionless extinction efficiency factor for randomly-oriented particles is

$$Q_{\text{ext,ran}}(\lambda) \equiv \frac{C_{\text{ext,ran}}(\lambda)}{\pi a_{\text{eff}}^2}, \quad (4)$$

where  $C_{\text{ext,ran}}(\lambda)$  is the extinction cross section averaged over random orientations.

Let  $\hat{\mathbf{a}}_1$  be the principal axis of largest moment of inertia, and let  $\mathbf{J}$  be the grain’s angular momentum. The idealized case of “perfect spinning alignment” (PSA) has the grains spinning with  $\hat{\mathbf{a}}_1 \parallel \mathbf{J}$ , and  $\mathbf{J} \parallel \mathbf{B}_0$ , where  $\mathbf{B}_0$  is the local magnetic field (see Figure 3). The extinction cross section will depend on the orientation of the rotation axis  $\hat{\mathbf{a}}_1$  relative to the line of sight. Let  $\hat{\mathbf{x}}$  and  $\hat{\mathbf{y}}$  be unit vectors perpendicular to the line of sight. We consider the limiting case where  $\mathbf{B}_0$  is “in the plane of the sky”, with  $\mathbf{B}_0 \parallel \hat{\mathbf{x}}$ , thus  $\hat{\mathbf{a}}_1 \parallel \hat{\mathbf{x}}$  (see Figure 3). The dimensionless efficiency factors for polarization and extinction for grains in PSA are defined to be

$$Q_{\text{pol,PSA}}(\lambda) \equiv \frac{\langle C_{\text{ext},y}(\lambda) - C_{\text{ext},x}(\lambda) \rangle_{\text{PSA}}}{2\pi a_{\text{eff}}^2} \quad (5)$$

$$Q_{\text{ext,PSA}}(\lambda) \equiv \frac{\langle C_{\text{ext},y}(\lambda) + C_{\text{ext},x}(\lambda) \rangle_{\text{PSA}}}{2\pi a_{\text{eff}}^2}, \quad (6)$$

where  $C_{\text{ext},x}$  and  $C_{\text{ext},y}$  are extinction cross sections for radiation with  $\mathbf{E}_{\text{inc}} \parallel \hat{\mathbf{x}}$  and  $\mathbf{E}_{\text{inc}} \parallel \hat{\mathbf{y}}$ , respectively, and  $\langle \dots \rangle_{\text{PSA}}$  denotes averaging over rotations of the grain around  $\hat{\mathbf{a}}_1 \parallel \hat{\mathbf{x}}$ .



## 5. DISCRETE DIPOLE APPROXIMATION

The discrete dipole approximation (DDA) is a finite element approximation for solving Maxwell’s equations for a chosen target geometry (Purcell & Pennypacker 1973; Draine 1988; Draine & Flatau 1994). The public domain DDA program DDSCAT<sup>1</sup> is used to calculate scattering and absorption. The geometries considered here are among the shape options available within DDSCAT.

DDSCAT approximates a target by an array of  $N$  polarizable points (referred to as “dipoles”) located on a cubic lattice with lattice spacing  $d$ . Lattice points are included in the target array if the point falls within the volume  $V$  defined by the ideal target shape; the choice of lattice spacing  $d$  determines the number of dipoles  $N \approx V/d^3$ . For symmetric targets, DDSCAT sets the target symmetry axis to be parallel to one of the lattice axes, with the target centroid offset by  $(\delta_x, \delta_y, \delta_z)d$  from the nearest lattice point. For all shapes considered here, DDSCAT uses offsets  $(\delta_x, \delta_y, \delta_z) = (0.5, 0.5, 0.5)$ . Each polarizable point has a prescribed complex polarizability  $\tilde{\alpha}_j(\lambda)$ . The “lattice dispersion relation” prescription (Draine & Goodman 1993; Gutkowitz-Krusin & Draine 2004) is used to determine the  $\tilde{\alpha}_j(\lambda)$  appropriate for modeling material with specified complex dielectric function  $\epsilon(\lambda)$ .

For finite  $N$ , the ideal target geometry is imperfectly reproduced by the dipole array, but the method converges to the ideal geometry in the limit  $N \rightarrow \infty$ . Figure 1 shows DDA realizations using  $N \approx 10^5$  for the 20 convex targets. Light scattering calculations are carried out using even larger numbers of dipoles (see Table 3) in order to more closely approximate the ideal target shapes, and to adequately resolve the electromagnetic field even for vacuum wavelengths as short as  $0.1\mu\text{m}$ .

For an incoming polarized monochromatic plane wave, DDSCAT iteratively converges on the self-consistent solution for the  $N$  oscillating dipole polarizations  $\mathbf{P}_j$ . From the solution  $\mathbf{P}_j$ , scattering and absorption cross sections are calculated.

Let  $\hat{\mathbf{k}}$  be the direction of propagation of the incident plane wave, and let  $\hat{\mathbf{a}}$  be an axis fixed in the grain (if the grain has rotational symmetry, it is convenient to choose  $\hat{\mathbf{a}}$  to be the symmetry axis). The electromagnetic scattering problem depends on the angle  $\Theta$  between  $\hat{\mathbf{a}}$  and  $\hat{\mathbf{k}}$ , and on the linear polarization  $\mathbf{E}_{\text{inc}}$  of the incident wave. For non-axisymmetric targets, the problem also depends on an angle  $\beta$  specifying rotation of the target around the target axis  $\hat{\mathbf{a}}$ . Let  $C_E(\Theta, \beta, \lambda)$  be the cross sections for  $\mathbf{E}_{\text{inc}}$  in the  $\hat{\mathbf{k}} - \hat{\mathbf{a}}$  plane, and  $C_H(\Theta, \beta, \lambda)$  the cross section for  $\mathbf{E}_{\text{inc}}$  perpendicular to the  $\hat{\mathbf{k}} - \hat{\mathbf{a}}$  plane. Cross sections are given in terms of dimensionless efficiency factors  $Q \equiv C/\pi a_{\text{eff}}^2$ .

For each of the target shapes and sizes, the scattering problem is solved for 151 values of  $\lambda$ , uniformly spaced in  $\log(\lambda)$  from  $\lambda = 0.1\mu\text{m}$  to  $100\mu\text{m}$ . The 20 shapes considered here all have reflection symmetry through a plane perpendicular to  $\hat{\mathbf{a}}$ ; thus we need to consider only  $\Theta \in [0, 90^\circ]$ . We use 11 values of  $\Theta$  (uniformly spaced in  $\cos \Theta$  from 0 to 1). For the axisymmetric shapes,  $\beta$  is irrelevant. For the rectangular prisms, we use 3 values of  $\beta \in (0, 45^\circ)$ :  $7.5^\circ, 22.5^\circ, 37.5^\circ$ . For the triaxial ellipsoids, we choose  $\hat{\mathbf{a}} = \hat{\mathbf{a}}_1$ , and use 3 values of  $\beta \in (0, 90^\circ)$ :  $15^\circ, 45^\circ, 75^\circ$ .

### 5.1. $N \rightarrow \infty$ Extrapolation and Uncertainties $|\Delta Q|$

The errors in the DDA are primarily associated with the polarizations of the dipoles near the target surface. Let  $D$  be some characteristic dimension of the target. Because the fraction of the dipole sites that are within a distance  $d$  of the surface scales as  $d/D$ , the fractional error depends on  $d/D$ . As discussed by Collinge & Draine (2004), because  $N \propto (D/d)^3$ , the fractional error is expected to scale as  $N^{-1/3}$ . Thus if  $Q_\infty$  is the exact result,

$$Q_N \approx Q_\infty + AN^{-1/3} \quad , \quad (7)$$

<sup>1</sup> DDSCAT version 7.3.3, available at [www.ddscat.org](http://www.ddscat.org).

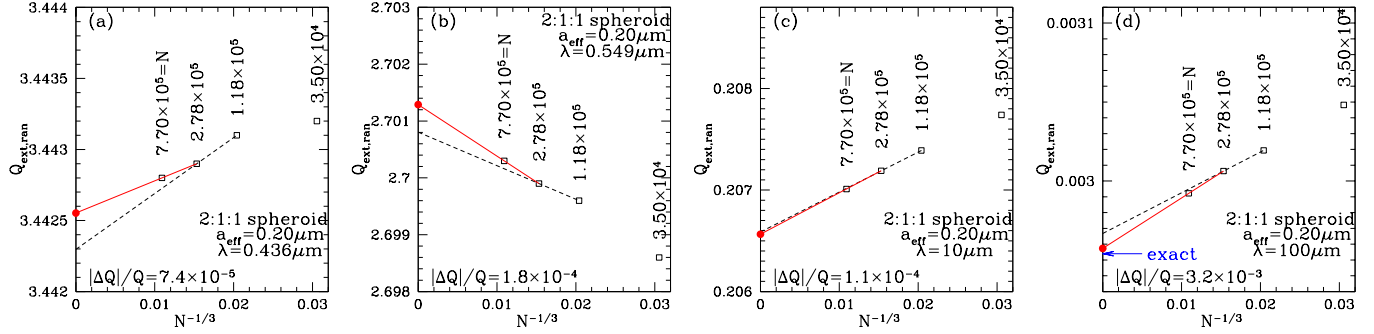


**Figure 4.** DDA calculations of  $Q_{\text{ext,ran}}$  for randomly-oriented 2:1:1 spheroids with volume-equivalent radii  $a_{\text{eff}} = 0.20\mu\text{m}$  as a function of  $N^{-1/3}$ , where  $N$  is the number of dipoles. The “prolate” dielectric function from Figure 2 is assumed. Results are shown for four wavelengths  $\lambda$ . For each  $\lambda$ , extrapolations to  $Q_{\infty}$  are made using the results for the two largest values of  $N$  (solid line) and using the second and third largest values of  $N$  (dashed line). The magnitude  $|\Delta Q|$  of the difference between these two extrapolations is a reasonable estimate for the uncertainty in the estimate for  $Q_{\infty}$ . The fractional uncertainty ranges from  $\sim 7 \times 10^{-5}$  at  $\lambda = 0.44\mu\text{m}$  to  $\sim 3 \times 10^{-3}$  at  $\lambda = 100\mu\text{m}$ . The exact result in the Rayleigh limit is shown for  $\lambda = 100\mu\text{m}$  in (d); agreement is excellent.

where  $A$  is some constant. If we calculate  $Q_N$  for  $N = N_1$  and  $N_2$ , we can extrapolate to estimate  $Q_{\infty}$  (Shen et al. 2008):

$$Q_{\infty}(N_1, N_2) \approx Q_{N_1} - \frac{Q_{N_1} - Q_{N_2}}{1 - (N_1/N_2)^{1/3}} \quad . \quad (8)$$

In Appendix B we test Equation (8) using a test case – spheres – where DDA calculations can be compared to exact results obtained from Mie theory (see, e.g., Bohren & Huffman 1983). Equation (8) is found to give very accurate results.

Because Equation (7) is only an approximation to the actual variation of  $Q$  with  $N$ , the estimate (8) for  $Q_{\infty}$  will not be exact. The uncertainty in this estimate can itself be estimated by calculating  $Q_N$  for three values  $N_1 > N_2 > N_3$ , and comparing the extrapolation (8) using  $N_1$  and  $N_2$  with the result using  $N_2$  and  $N_3$ : the difference is

$$\Delta Q \equiv Q_{\infty}(N_1, N_2) - Q_{\infty}(N_2, N_3) = \frac{(Q_{N_1} - Q_{N_2})}{1 - (N_2/N_1)^{1/3}} + \frac{(Q_{N_2} - Q_{N_3})}{1 - (N_2/N_3)^{1/3}} \quad . \quad (9)$$

$|\Delta Q|$  is a reasonable estimate for the magnitude in the uncertainty in the estimate of  $Q_{\infty}$ .

Figure 4 shows efficiency factors  $Q_{\text{ext,ran}}(\lambda)$  for randomly-oriented 2:1:1 prolate spheroids as a function of  $N^{-1/3}$  for  $a_{\text{eff}} = 0.20\mu\text{m}$  and 4 wavelengths  $\lambda$ :  $0.437\mu\text{m}$ ,  $0.550\mu\text{m}$ ,  $10\mu\text{m}$ , and  $100\mu\text{m}$ . Results are shown for 4 values of  $N$ , ranging from  $\sim 3.5 \times 10^4$  to  $\sim 7.7 \times 10^5$ . Extrapolations using the largest two values of  $N$  (solid line) and using the second and third largest values of  $N$  (dashed line) are shown. The fractional uncertainty estimate  $|\Delta Q|/Q$  in extrapolation of  $Q_{\text{ext,ran}}$  to  $N \rightarrow \infty$  (see Equation 9) is given for each example.

At optical wavelengths the DDA results are very accurate, with fractional uncertainties  $|\Delta Q|/Q \sim 7 \times 10^{-5}$  and  $2 \times 10^{-4}$  at  $\lambda = 0.44\mu\text{m}$  and  $0.55\mu\text{m}$ . At  $10\mu\text{m}$  the fractional uncertainty is also small,  $\sim 1 \times 10^{-4}$ . However, as the dielectric function  $\epsilon$  becomes large in the FIR (see Figure 2), the DDA becomes less accurate; for the spheroidal shape, the estimated fractional uncertainty in  $Q_{\text{ext,ran}}$  increases to  $\sim 3 \times 10^{-3}$  at  $\lambda = 100\mu\text{m}$ . However, at  $\lambda = 100\mu\text{m}$  the grains are in the Rayleigh limit, and we can compare with the analytic result for spheroids (see, e.g. Bohren & Huffman 1983). Figure 4d shows that the agreement is excellent; Equation (9) evidently overestimates the uncertainty. To verify that this behavior is general, similar results for 2:1:1 cylinders can be found in Appendix B.



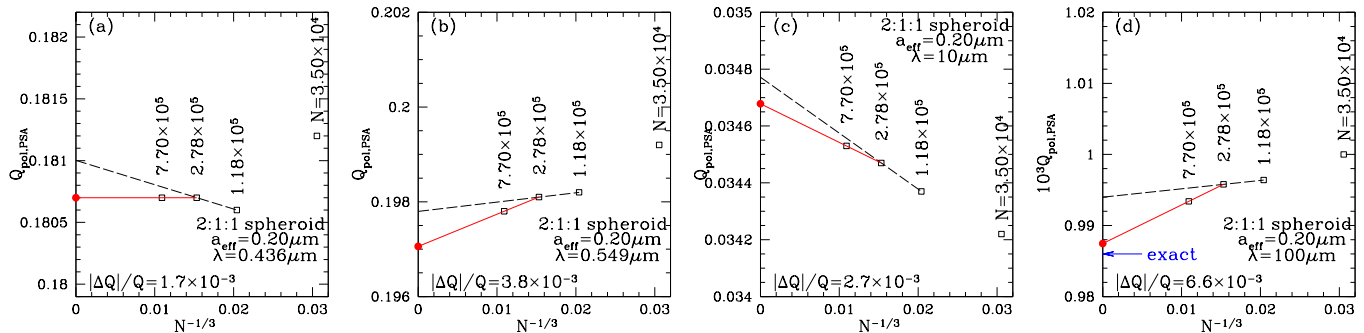


**Figure 5.** DDA calculations of  $Q_{\text{pol,PSA}}$  for 2:1:1 prolate spheroids with volume-equivalent radii  $a_{\text{eff}} = 0.20\mu\text{m}$  as a function of  $N^{-1/3}$ , where  $N$  is the number of dipoles used to represent the target. The “prolate” dielectric function from Figure 2 is used. Results are shown for four wavelengths. The exact result in the Rayleigh limit is shown for  $\lambda = 100\mu\text{m}$  in (d); agreement is excellent.

Figure 5 shows  $Q_{\text{pol,PSA}}$  as a function of  $N^{-1/3}$ , calculated for  $a_{\text{eff}} = 0.2\mu\text{m}$  2:1:1 spheroids, for four selected wavelengths. In each case we extrapolate to  $N \rightarrow \infty$ . The fractional uncertainties  $\Delta Q_{\text{pol,PSA}}/Q_{\text{pol,PSA}}$  (given in each panel of Figure 5) are larger than the fractional uncertainties in  $Q_{\text{ext,ran}}$  (given in each panel of Figure 4), but are still relatively small at the optical wavelengths that are important for starlight polarization: less than 1% at  $\lambda = 0.55\mu\text{m}$  for most cases. Similar plots of  $Q_{\text{pol,PSA}}$  vs.  $N^{-1/3}$  for 2:1:1 cylinders can be found in Appendix B.

## 6. EXTINCTION AND POLARIZATION BY NONSPHERICAL GRAINS

### 6.1. Extinction Cross Sections

Figure 6 shows the full  $\lambda$ -dependence of the dimensionless quantity  $\lambda Q_{\text{ext,ran}}(\lambda)/a_{\text{eff}}$  for eight of the shapes from Figure 1, for four different grain sizes ( $a_{\text{eff}} = 0.05, 0.1, 0.2, 0.3\mu\text{m}$ ). The eight selected shapes consist of four flattened and four elongated geometries from Figure 1. The chosen examples all have flattenings or elongations sufficient to reproduce the observed polarization of starlight.

For all cases, the quantity  $\lambda Q_{\text{ext,ran}}/a_{\text{eff}}$  peaks near  $\lambda \approx 2.5a_{\text{eff}}$ , or  $2\pi a_{\text{eff}}/\lambda \approx 2.5$ . For  $\lambda \gtrsim 5\mu\text{m}$ , the grain sizes  $a \leq 0.3\mu\text{m}$  considered here are in the Rayleigh limit  $a_{\text{eff}} \ll \lambda$ , absorption cross section per unit volume become independent of particle size, and  $\lambda Q_{\text{ext,ran}}/a_{\text{eff}}$  becomes independent of  $a_{\text{eff}}$ , as seen in Figure 6.

### 6.2. Polarization Cross Sections

Figure 7 shows the dimensionless quantity  $\lambda Q_{\text{pol,PSA}}/a_{\text{eff}}$  for the eight shapes in Figure 6, for four grain sizes.  $\lambda Q_{\text{pol,PSA}}/a_{\text{eff}}$  peaks at  $\lambda \approx 3a_{\text{eff}}$ , with  $Q_{\text{pol,PSA}}$  itself peaking near  $\lambda \approx 2.5a_{\text{eff}}$  – thus the observed peak in starlight polarization near  $\lambda \approx 0.55\mu\text{m}$  must be due to grains with  $a_{\text{eff}} \approx 0.2\mu\text{m}$ .

The eight shapes considered here have similar extinction curves, as seen in Figure 6. The polarization profiles in Figure 7 are broadly similar to one another, but do differ from shape to shape. For example, it is clear from Figure 7 that the 2:1:1 cylinder (Figure 7f) has enhanced polarization at FIR wavelengths relative to the 5:7:7 spheroid (Figure 7a). We will examine this further below.

## 7. POLARIZATION OF STARLIGHT: OBSERVATIONAL CONSTRAINTS

The observed wavelength dependence of starlight polarization is approximated by the fitting function found by Serkowski (1973):

$$p_{\text{obs}}(\lambda) \approx p_{\text{max}} \exp \left[ -K (\ln(\lambda/\lambda_{\text{max}}))^2 \right] \quad , \quad (10)$$

with  $p_{\text{max}}$  the polarization at the wavelength  $\lambda_{\text{max}}$  where the polarization peaks. Typical sightlines have  $\lambda_{\text{max}} \approx 0.55\mu\text{m}$  and  $K \approx 0.87$  (Serkowski et al. 1975; Whittet et al. 1992; Martin et al.

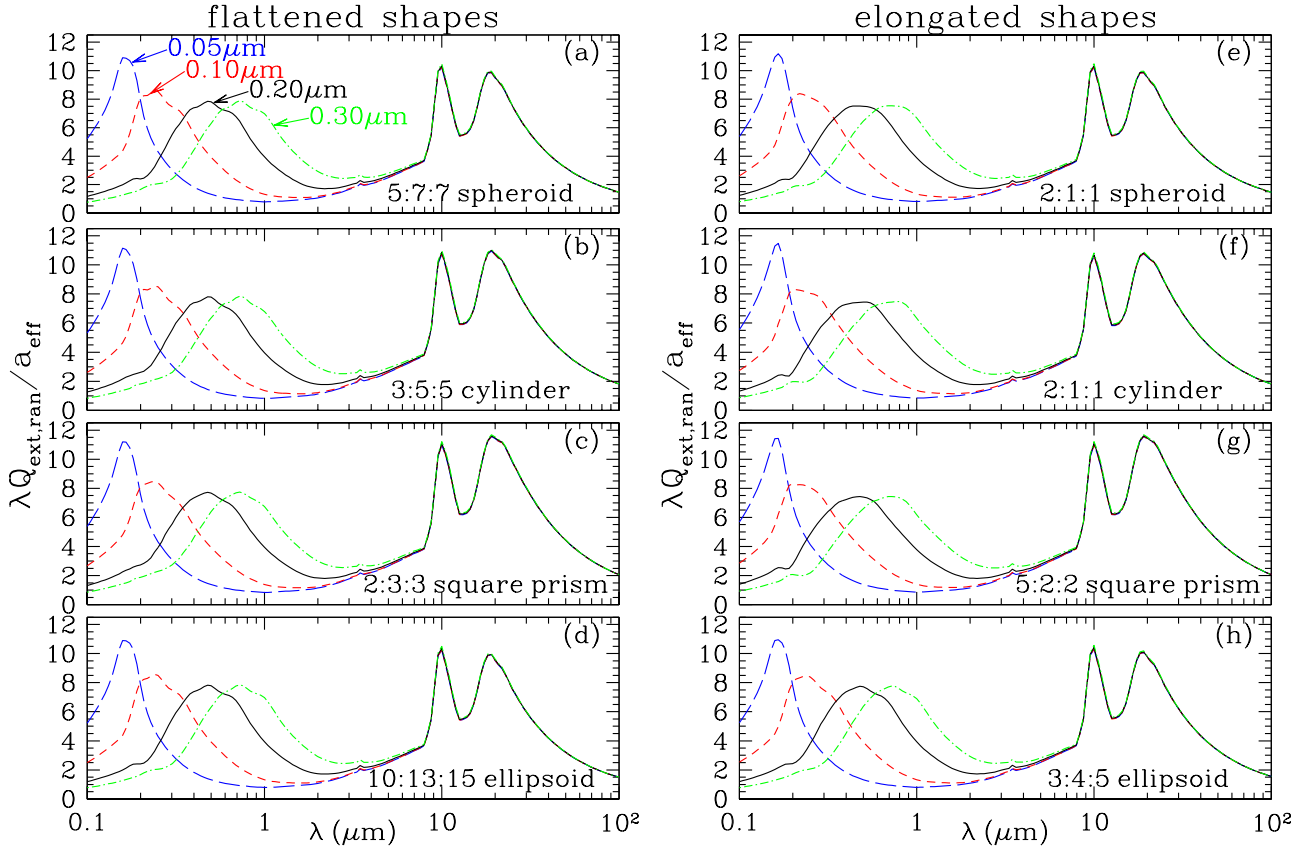


**Figure 6.**  $\lambda Q_{\text{ext,ran}}/a_{\text{eff}}$  as a function of wavelength  $\lambda$  for (a) 5:7:7 oblate spheroids, (b) 3:5:5 cylinders, (c) 2:3:3 square prisms, (d) 10:13:15 ellipsoids, (e) 2:1:1 prolate spheroids, (f) 2:1:1 cylinders, (g) 5:2:2 square prisms, and (h) 3:4:5 ellipsoids, for  $a_{\text{eff}} = 0.05, 0.10, 0.20, 0.30 \mu\text{m}$ . Flattened shapes use the “oblate” dielectric function shown in Figure 2; elongated shapes use the “prolate” dielectric function from Figure 2 (see text). Cross sections are extrapolated using Equation (8) for  $N_1, N_2$  in Table 3.

1999; Whittet 2022). Starlight polarization is strongest and best observed over the wavelength range  $0.15 \mu\text{m} \lesssim \lambda \lesssim 2.5 \mu\text{m}$ , and the “Serkowski law” (10) provides a good approximation over this interval. We concentrate attention on the wavelength range  $[\lambda_1, \lambda_2]$ , with  $\lambda_1 = 0.15 \mu\text{m}$  and  $\lambda_2 = 2.5 \mu\text{m}$ .

Define an effective wavelength for the observed starlight polarization over  $[\lambda_1, \lambda_2]$ :

$$\lambda_{p,\text{obs}} \equiv \exp \left\{ \frac{\int_{\lambda_1}^{\lambda_2} \ln \lambda p_{\text{obs}}(\lambda) d \ln \lambda}{\int_{\lambda_1}^{\lambda_2} p_{\text{obs}}(\lambda) d \ln \lambda} \right\} \approx 0.567 \mu\text{m} \quad (11)$$

for  $p_{\text{obs}}(\lambda)$  given by Equation (10),  $\lambda_{\text{max}} = 0.55 \mu\text{m}$ , and  $K = 0.87$ ;  $\lambda_{p,\text{obs}}$  is close to (but not identical to) the wavelength  $\lambda_{\text{max}}$  of peak polarization. The width of the starlight polarization profile is characterized by

$$\sigma_{\text{obs}}^2 \equiv \frac{\int_{\lambda_1}^{\lambda_2} [\ln(\lambda/\lambda_{p,\text{obs}})]^2 p_{\text{obs}}(\lambda) d \ln \lambda}{\int_{\lambda_1}^{\lambda_2} p_{\text{obs}}(\lambda) d \ln \lambda} \approx (0.64)^2 \quad (12)$$

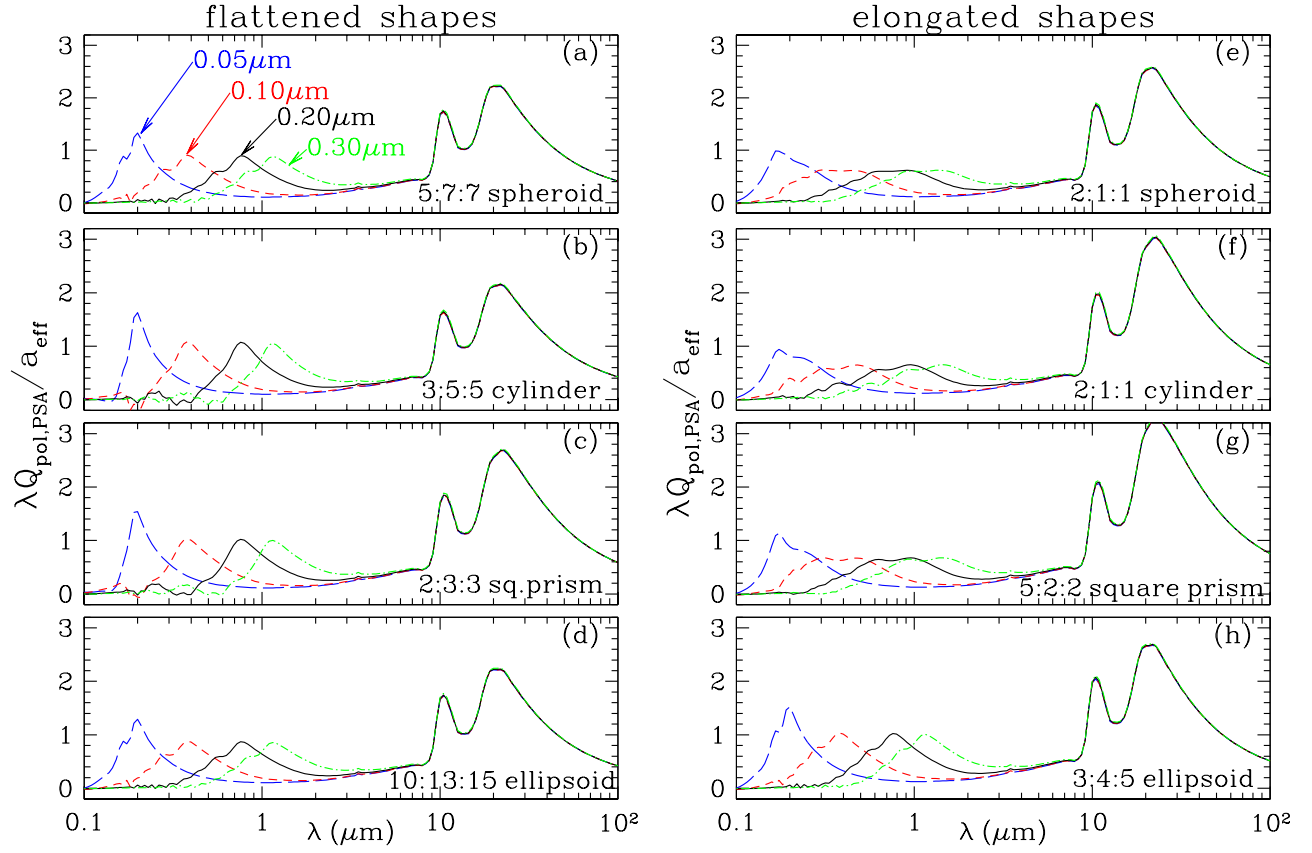


**Figure 7.** As in Figure 6, but showing  $\lambda Q_{\text{pol,PSA}}/a_{\text{eff}}$  as a function of wavelength  $\lambda$  for perfect spinning alignment.

The strength of the starlight polarization reaches values as high as<sup>2</sup>

$$\left(\frac{p_{\text{max}}}{N_{\text{H}}}\right)_{\text{max}} = 1.48 \times 10^{-23} \text{ cm}^2 \text{H}^{-1} . \quad (13)$$

From Equations (10) and (13), the observed starlight polarization integral per H is

$$\left(\frac{\Pi_{\text{obs}}}{N_{\text{H}}}\right)_{\text{max}} \equiv \int_{\lambda_1}^{\lambda_2} \left(\frac{p_{\text{obs}}(\lambda)}{N_{\text{H}}}\right)_{\text{max}} d\lambda \approx 1.23 \mu\text{m} \left(\frac{p_{\text{max}}}{N_{\text{H}}}\right)_{\text{max}} \approx 1.82 \times 10^{-27} \text{ cm}^3 \text{H}^{-1} \quad (14)$$

(Draine & Hensley 2021b).

At intermediate or high galactic latitudes, the volume of grain material per H nucleon is estimated to be (Draine & Hensley 2021a)

$$V_{\text{gr}} \approx \frac{3.0 \times 10^{-27} \text{ cm}^3 \text{H}^{-1}}{1 - \mathcal{P}_{\text{micro}}} , \quad (15)$$

where the “microporosity”  $\mathcal{P}_{\text{micro}}$  is the vacuum fraction on very small scales. Observations of starlight polarization and polarized submm emission both suggest that the porosity is not high (see Draine &

<sup>2</sup> For  $[p_{\text{max}}/E(B-V)]_{\text{max}} = 0.13 \text{ mag}^{-1}$  (Panopoulou et al. 2019; Planck Collaboration et al. 2020) and  $N_{\text{H}}/E(B-V) = 8.8 \times 10^{21} \text{ cm}^2 \text{ mag}^{-1}$  (Lenz et al. 2017).

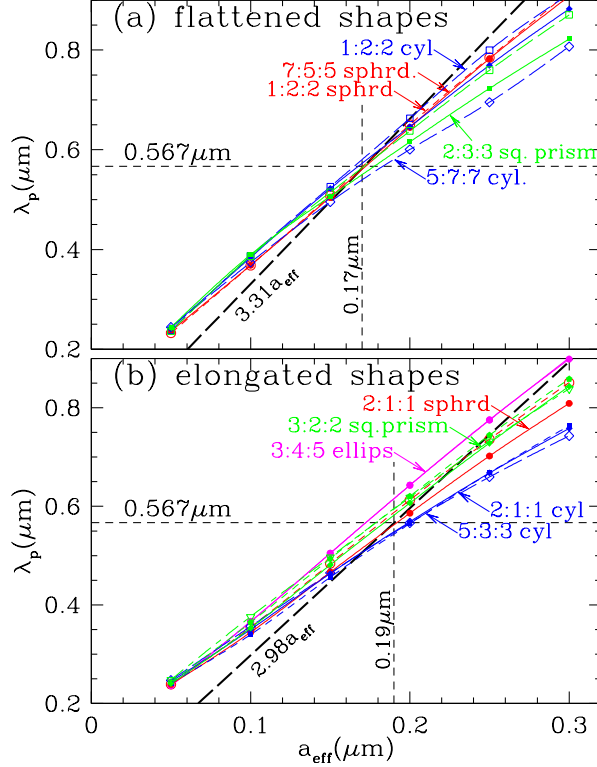


**Figure 8.** Effective wavelength for polarization  $\lambda_p(a_{\text{eff}})$  for (a) 10 flattened and (b) 10 elongated grain shapes studied here. Some of the outliers are labelled. The grains dominating starlight polarization should have  $\lambda_p \approx 0.567\mu\text{m}$ , corresponding to  $a_{\text{eff}} \sim 0.17\mu\text{m}$  for the flattened shapes, or  $\sim 0.19\mu\text{m}$  for the elongated shapes. *[btd note: 8.pdf]*

Hensley 2021b). Here we set  $\mathcal{P}_{\text{micro}} = 0.2$ , the value favored by Hensley & Draine (2023). Thus the interstellar dust population must be consistent with

$$\left( \frac{\Pi_{\text{obs}}}{N_{\text{H}}} \right)_{\text{max}} \frac{1}{V_{\text{gr}}} \approx 0.49 \quad . \quad (16)$$

A viable model for interstellar dust should reproduce the full observed wavelength dependence of extinction and polarization, both of which are sensitive to the grain size distribution  $dn_d/da_{\text{eff}}$ , with polarization also sensitive to the fractional alignment  $f_{\text{align}}(a_{\text{eff}}) \leq 1$  of the particles. Models of interstellar polarization must reproduce the effective wavelength  $\lambda_{p,\text{obs}}$  (Eq. 11), the profile width  $\sigma_{\text{obs}}$  (Eq. 12), and the observed strength per grain volume (Eq. 16). However, the starlight polarization has some integrated properties that are relatively insensitive to grain size – the starlight polarization integral per grain volume  $\Pi_{\text{obs}}/N_{\text{H}}V_{\text{gr}}$  (see Eq. 16) and the fractional width  $\sigma_{\text{obs}}$  of the starlight polarization profile (see Eq. 12).

## 8. EFFECTIVE WAVELENGTH AND WIDTH OF POLARIZATION BY GRAINS

The effective wavelength  $\lambda_p$  for the polarization contribution of grains of a given shape and size  $a_{\text{eff}}$  is (Draine & Hensley 2021b):

$$\lambda_p(\text{shape}, a_{\text{eff}}) \equiv \exp \left\{ \frac{\int_{\lambda_1}^{\lambda_2} (\ln \lambda) Q_{\text{pol,PSA}}(\text{shape}, a_{\text{eff}}, \lambda) d \ln \lambda}{\int_{\lambda_1}^{\lambda_2} Q_{\text{pol,PSA}}(\text{shape}, a_{\text{eff}}, \lambda) d \ln \lambda} \right\} \quad . \quad (17)$$

Figure 8 shows  $\lambda_p$  as a function of  $a_{\text{eff}}$  for the 20 shapes studied here. The flattened ( $\mathcal{S} < 1$ ) shapes in Figure 9a have

$$\lambda_p \approx 3.31a_{\text{eff}} \quad , \quad (18)$$

while the elongated ( $\mathcal{S} > 1$ ) shapes in Figure 9b have

$$\lambda_p \approx 2.98a_{\text{eff}} \quad . \quad (19)$$

As discussed above, the grains responsible for starlight polarization have  $\lambda_{p,\text{obs}} \approx 0.567\mu\text{m}$ . From Figure 9a,b we see that  $\lambda \approx 0.567\mu\text{m}$  corresponds to  $0.15 \lesssim a_{\text{eff}} \lesssim 0.20\mu\text{m}$  for the shapes considered here. For a single shape and size, the width of the starlight polarization profile can be characterized by

$$\sigma_p^2(\text{shape}, a_{\text{eff}}) \equiv \frac{\int_{\lambda_1}^{\lambda_2} d \ln \lambda [\ln(\lambda/\lambda_p)]^2 |Q_{\text{pol,PSA}}(\text{shape}, a_{\text{eff}}, \lambda)|}{\int_{\lambda_1}^{\lambda_2} d \ln \lambda |Q_{\text{pol,PSA}}(\text{shape}, a_{\text{eff}}, \lambda)|} \quad . \quad (20)$$

Because  $Q_{\text{pol,PSA}}$  can become negative on the short-wavelength wing of the polarization profile, we introduce the absolute value operator in Eq. (20) to avoid negative contributions to the integrals.

Table 1 gives  $\sigma_p$  for the shapes studied here. For each case, results are interpolated to the value of  $a_{\text{eff}}$  corresponding to  $\lambda_p = \lambda_{p,\text{obs}} = 0.567\mu\text{m}$ . The uncertainties listed for  $\sigma_p$  are based on Eq. (9), using sizes  $N_1, N_2, N_3$  in Table 3.

Individual grains do not reproduce the Serkowski law (10) – the Serkowski law arises after summing over a range of grain sizes. Because  $\lambda_p \propto a_{\text{eff}}$ , a model with a size distribution for the aligned grains will have  $\sigma_{\text{obs}} > \sigma_p(\text{shape}, a_{\text{eff},p})$ , where  $a_{\text{eff},p}$  is the size with  $\lambda_p = \lambda_{p,\text{obs}}$ . With  $\sigma_{\text{obs}} \approx 0.64$  for the Serkowski law (10) with the typical parameters ( $K = 0.87$ ,  $\lambda_p = 0.55\mu\text{m}$ ), a conservative upper limit  $\sigma_p < 0.60$  is chosen for compatibility with the observed starlight polarization. Hensley & Draine (2023) showed that a model using 5:7:7 oblate spheroids ( $\sigma_p = 0.516$ : see Table 1) with a suitable size distribution and alignment function can reproduce both the average extinction law and the observed starlight polarization.

After summing over a size distribution, shapes with  $\sigma_p > 0.60$  will result in a model polarization profile broader than observed. The condition  $\sigma_p < 0.60$  appears to rule out the 5:7:7 cylinder, the 2:3:3 square prism, the 5:3:3 cylinder, and the 2:1:1 cylinder (see Figure 9).

## 9. THE STARLIGHT POLARIZATION EFFICIENCY INTEGRAL

Consider now the strength of the observed polarization. Draine & Hensley (2021b) defined the starlight polarization efficiency integral:

$$\Phi(\text{shape}, a_{\text{eff}}, \gamma) \equiv \frac{1}{f_{\text{align}}(a_{\text{eff}}) \sin^2 \gamma} \int_{\lambda_1}^{\lambda_2} \frac{\langle C_{\text{ext},y}(\lambda) \rangle - \langle C_{\text{ext},x}(\lambda) \rangle}{2V} d\lambda \quad , \quad (21)$$

for radiation propagating in the  $\hat{z}$  direction and  $\mathbf{B}_0$  in the  $\hat{x} - \hat{z}$  plane;  $\gamma$  is the angle between the magnetic field and the  $\hat{z}$  axis,  $f_{\text{align}}(a_{\text{eff}})$  is the fractional alignment,<sup>3</sup> and  $\langle \dots \rangle$  denotes orientational average.

The starlight polarization efficiency integral  $\Phi$  is a dimensionless measure of the ability of a dust grain to contribute to starlight polarization. In principle,  $\Phi$  depends on both the magnetic field orientation  $\gamma$  and the distribution of grain alignments, but Draine & Hensley (2021b) showed that  $\Phi$  is nearly independent of both  $\gamma$  and the degree of grain alignment, both factors being effectively compensated for by the denominator  $f_{\text{align}} \sin^2 \gamma$  in Equation (21). Here we compute  $\Phi_{\text{PSA}}$  for perfect spinning alignment ( $f_{\text{align}} = 1$ ) and  $\mathbf{B}_0$  in the plane of the sky ( $\sin^2 \gamma = 1$ ):

$$\Phi_{\text{PSA}}(\text{shape}, a_{\text{eff}}) \equiv \int_{\lambda_1}^{\lambda_2} \frac{3Q_{\text{pol,PSA}}(\text{shape}, a_{\text{eff}}, \lambda)}{4a_{\text{eff}}} d\lambda \quad , \quad (22)$$

<sup>3</sup>  $f_{\text{align}}(a_{\text{eff}}) \equiv \langle (\hat{\mathbf{a}}_1 \cdot \hat{\mathbf{b}})^2 \rangle$ , where  $\hat{\mathbf{a}}_1$  is the principal axis of largest moment of inertia, and  $\hat{\mathbf{b}} \equiv \mathbf{B}_0/|\mathbf{B}_0|$ .

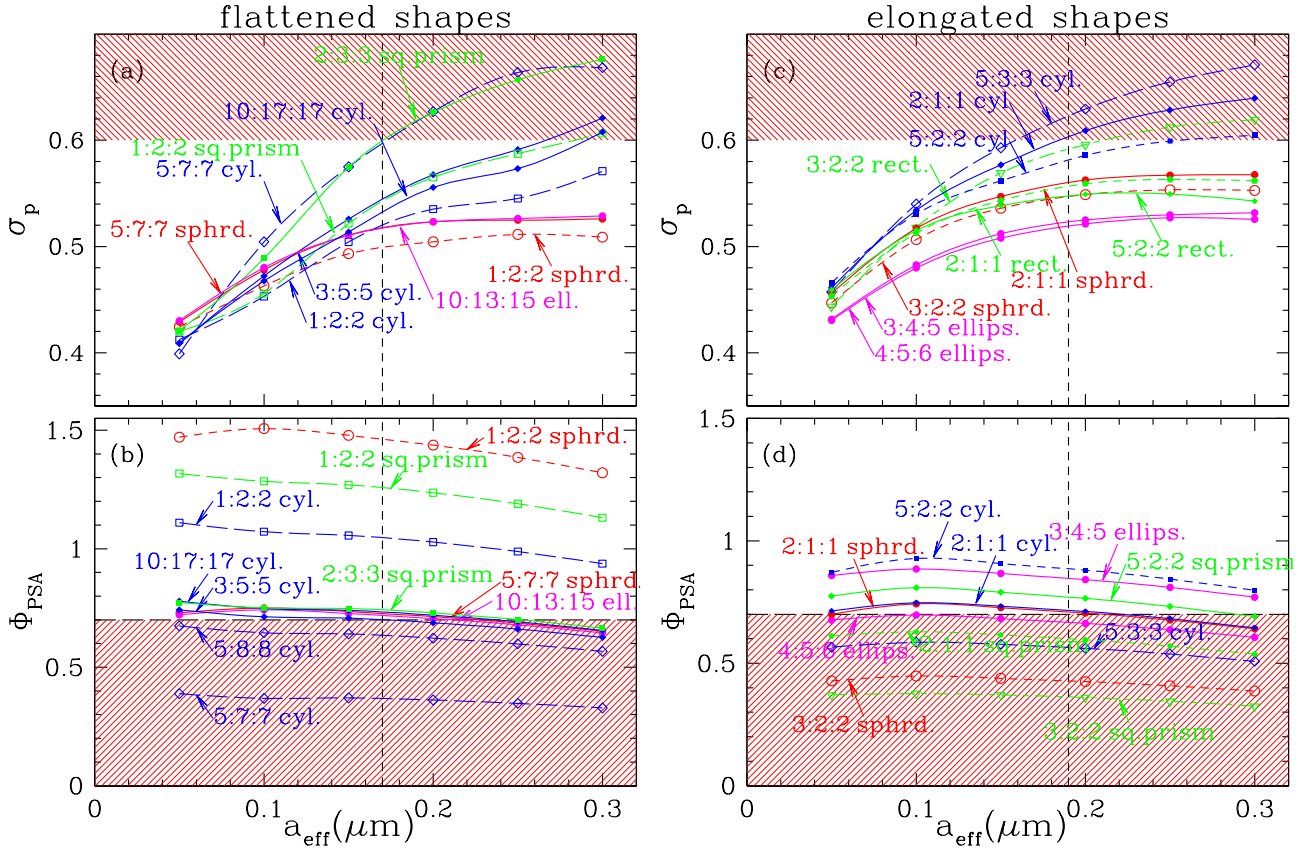


**Figure 9.** (a,c) Characteristic width  $\sigma_p$  of the polarization profile (see Equation 20) for different grain shapes, as a function of  $a_{\text{eff}}$ . The shaded region is forbidden by the observed width of the interstellar polarization (see text). (b,d) Polarization efficiency integral  $\Phi_{\text{PSA}}$  as a function of grain size  $a_{\text{eff}}$ . The shaded region is forbidden by Equation (26).

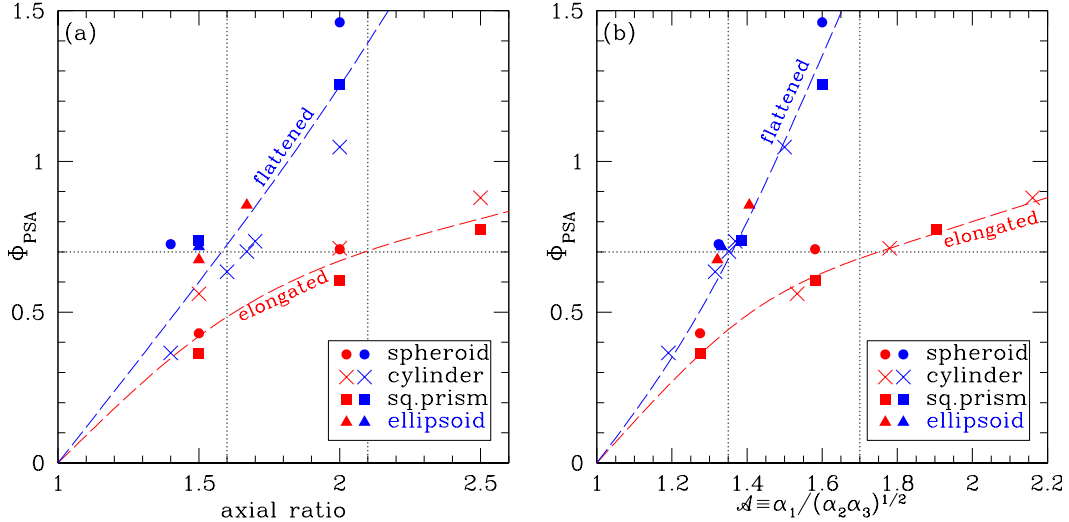


**Figure 10.** Starlight polarization efficiency  $\Phi_{\text{PSA}}$  vs. (a) axial ratio, and (b)  $\mathcal{A} \equiv \alpha_1 / (\alpha_2 \alpha_3)^{1/2}$  (Eq. 2). Values shown are for  $a_{\text{eff}} = 0.2 \mu\text{m}$  grains. Dashed curves show trends for flattened and elongated spheroids.



**Table 1.** Starlight Polarization Properties of Different Shapes

shape	$\mathcal{A}^a$	$\mathcal{S}^b$	Flattened Shapes ( $\mathcal{S} < 1$ )			comment
			$a_{\text{eff}}(\mu\text{m})$	$\sigma_p^c$	$\Phi_{\text{PSA}}^d$	
5:7:7 cylinder	1.1903	0.9166	0.184	$0.610 \pm 0.002$	$0.365 \pm 0.000$	$\Phi_{\text{PSA}}$ too small, $\sigma_p$ too large
5:8:8 cylinder	1.3151	0.8720	0.168	$0.549 \pm 0.008$	$0.634 \pm 0.020$	$\Phi_{\text{PSA}}$ too small
5:7:7 spheroid	1.3243	0.8690	0.172	$0.516 \pm 0.001$	$0.726 \pm 0.004$	
10:13:15 ellipsoid	1.3325	0.9983	0.172	$0.516 \pm 0.002$	$0.718 \pm 0.001$	
3:5:5 cylinder	1.3514	0.8602	0.165	$0.538 \pm 0.001$	$0.701 \pm 0.003$	
10:17:17 cylinder	1.3686	0.8548	0.163	$0.524 \pm 0.003$	$0.735 \pm 0.011$	
2:3:3 square prism	1.3846	0.8498	0.178	$0.603 \pm 0.000$	$0.738 \pm 0.000$	$\sigma_p$ too large
1:2:2 cylinder	1.5	0.8165	0.165	$0.514 \pm 0.004$	$1.048 \pm 0.019$	
1:2:2 spheroid	1.6	0.7906	0.171	$0.498 \pm 0.001$	$1.461 \pm 0.002$	
1:2:2 square prism	1.6	0.7906	0.171	$0.540 \pm 0.000$	$1.255 \pm 0.001$	
shape	$\mathcal{A}^a$	$\mathcal{S}^b$	Elongated Shapes ( $\mathcal{S} > 1$ )			comment
			$a_{\text{eff}}(\mu\text{m})$	$\sigma_p^c$	$\Phi_{\text{PSA}}^d$	
3:2:2 square prism	1.2748	1.2748	0.179	$0.585 \pm 0.001$	$0.364 \pm 0.002$	$\Phi_{\text{PSA}}$ too small
3:2:2 spheroid	1.2748	1.2748	0.182	$0.544 \pm 0.002$	$0.430 \pm 0.000$	$\Phi_{\text{PSA}}$ too small
4:5:6 ellipsoid	1.3211	1.0398	0.173	$0.518 \pm 0.001$	$0.674 \pm 0.003$	$\Phi_{\text{PSA}}$ too small
3:4:5 ellipsoid	1.4063	1.0620	0.173	$0.514 \pm 0.001$	$0.856 \pm 0.006$	
5:3:3 cylinder	1.5336	1.5336	0.200	$0.630 \pm 0.008$	$0.561 \pm 0.009$	$\Phi_{\text{PSA}}$ too small, $\sigma_p$ too large
2:1:1 square prism	1.5811	1.5811	0.179	$0.552 \pm 0.000$	$0.605 \pm 0.001$	$\Phi_{\text{PSA}}$ too small
2:1:1 spheroid	1.5811	1.5811	0.192	$0.560 \pm 0.000$	$0.709 \pm 0.002$	
2:1:1 cylinder	1.7795	1.7795	0.199	$0.609 \pm 0.007$	$0.712 \pm 0.011$	$\sigma_p$ too large
5:2:2 square prism	1.9039	1.9039	0.184	$0.546 \pm 0.000$	$0.773 \pm 0.001$	
5:2:2 cylinder	2.1602	2.1602	0.201	$0.586 \pm 0.025$	$0.880 \pm 0.014$	

*a* Asymmetry parameter (Eq. 2).

*b* Stretch parameter (Eq. 3).

*c* Polarization broadening parameter (Eq. 20).

*d* Polarization efficiency integral (Eq. 22).

with  $Q_{\text{pol,PSA}}$  defined by Equation (5). Figure 9 shows  $\Phi_{\text{PSA}}$  as a function of  $a_{\text{eff}}$  for the 20 shapes considered here, for the dielectric functions of Figure 2. As previously noted by Draine & Hensley (2021b) for spheroids,  $\Phi_{\text{PSA}}$  is sensitive to the grain shape, but is nearly independent of size  $a_{\text{eff}}$  for  $0.1\mu\text{m} < a_{\text{eff}} < 0.3\mu\text{m}$  – the range of grain sizes primarily responsible for the observed polarization of starlight.

Can one estimate  $\Phi_{\text{PSA}}$  from a simple measure of the geometric shape, such as the axial ratio, or the asymmetry parameter  $\mathcal{A}$  defined by Eq. (2)? Figure 10a shows how  $\Phi_{\text{PSA}}$  depends on axial ratio, while Figure 10b shows  $\Phi_{\text{PSA}}$  versus  $\mathcal{A}$ .  $\Phi_{\text{PSA}}$  tends to increase with increasing axial ratio, or increasing asymmetry parameter  $\mathcal{A}$ . If we separate the shapes into flattened ( $\mathcal{S} < 1$ ) and elongated ( $\mathcal{S} > 1$ ), we see that the axial ratio is a fair predictor of  $\Phi_{\text{PSA}}$ , but  $\Phi_{\text{PSA}}$  seems to show an even tighter correlation with  $\mathcal{A}$ .<sup>4</sup>

<sup>4</sup> The two “outliers” in Figure 10b are triaxial ellipsoids with  $\mathcal{S} = 1.04$  and 1.06 that seem to fall on the “flattened” track.

$\Phi_{\text{PSA}}$  is calculated for grains spinning around the principal axis of largest moment of inertia (i.e., “shortest” axis), as expected for suprathermal rotation. For a given axial ratio, flattened shapes (with one short axis and two long axes) tend to have larger  $\Phi_{\text{PSA}}$  than elongated shapes (with two short axes and one long axis).

## 10. DISCUSSION

### 10.1. Constraints on Grain Shape from Starlight Polarization

The observed polarization integral  $\Pi_{\text{obs}}$  is proportional to the mass-weighted fractional alignment  $\langle f_{\text{align}} \rangle$ , the dust volume per H  $V_{\text{gr}}$ , and the polarization efficiency integral  $\Phi_{\text{PSA}}$ :

$$\Pi_{\text{obs}} = \langle f_{\text{align}} \rangle V_{\text{gr}} \Phi_{\text{PSA}} \quad . \quad (23)$$

Combining Equations (16) and (23), we obtain

$$\langle f_{\text{align}} \rangle \Phi_{\text{PSA}} \approx 0.49 \quad . \quad (24)$$

The observed extinction curve rises steeply into the FUV; models seeking to reproduce this rise (e.g., Mathis et al. 1977) require  $\sim 30\%$  of the dust mass in grains with  $a_{\text{eff}} < 0.1\mu\text{m}$ . However, starlight polarization is weak in the FUV; the Serkowski law (10) can only be reproduced if grains with  $a_{\text{eff}} \lesssim 0.1\mu\text{m}$  contribute minimally to the polarization. If all grains have the same shape, then the small ( $a_{\text{eff}} \lesssim 0.1\mu\text{m}$ ) grains cannot be appreciably aligned; this implies that

$$\langle f_{\text{align}} \rangle \lesssim 0.7 \quad . \quad (25)$$

Thus, the grains responsible for starlight polarization must have

$$\Phi_{\text{PSA}} = \frac{0.49}{\langle f_{\text{align}} \rangle} \gtrsim 0.70 \quad . \quad (26)$$

**Table 2.** Infrared Polarization Properties for Shapes with  $\Phi_{\text{PSA}} > 0.7$ ,  $\sigma_p < 0.6$

shape	$\Phi_{\text{PSA}}^a$	$\sigma_p^a$	$[p_{\text{em}}(\text{FIR})]_{\text{max}}^b$	$\left[ \frac{C_{\text{pol,PSA}}(10\text{--}11\mu\text{m})}{V\Phi_{\text{PSA}}} \right]^c$ ( $\text{cm}^{-1}$ )	$\left[ \frac{\Delta C_{\text{pol,PSA}}(\text{sil.})}{V\Phi_{\text{PSA}}} \right]^d$ ( $\text{cm}^{-1}$ )	comment
3:5:5 cylinder	0.701	0.538	$0.1746 \pm 0.0000$	$1632 \pm 5$	$1025 \pm 2$	$[p_{\text{em}}(\text{FIR})]_{\text{max}}$ too small
<b>2:1:1 spheroid</b>	0.709	0.560	$0.2500 \pm 0.0001$	$1830 \pm 2$	$1225 \pm 2$	OK
<b>10:13:15 ellipsoid</b>	0.718	0.516	$0.2050 \pm 0.0001$	$1688 \pm 5$	$1082 \pm 5$	OK
10:17:17 cylinder	0.735	0.524	$0.1744 \pm 0.0002$	$1627 \pm 8$	$1023 \pm 8$	$[p_{\text{em}}(\text{FIR})]_{\text{max}}$ too small
<b>5:7:7 spheroid</b>	0.736	0.516	$0.2015 \pm 0.0003$	$1682 \pm 1$	$1075 \pm 3$	OK
<b>5:2:2 square prism</b>	0.773	0.546	$0.2495 \pm 0.0003$	$1835 \pm 1$	$1246 \pm 1$	OK
<b>3:4:5 ellipsoid</b>	0.856	0.514	$0.2014 \pm 0.0006$	$1677 \pm 18$	$1060 \pm 37$	OK
5:2:2 cylinder	0.880	0.586	$0.2652 \pm 0.0008$	$1897 \pm 9$	$1305 \pm 3$	$[p_{\text{em}}(\text{FIR})]_{\text{max}}$ too large
1:2:2 cylinder	1.048	0.514	$0.1710 \pm 0.0001$	$1641 \pm 1$	$1037 \pm 1$	$[p_{\text{em}}(\text{FIR})]_{\text{max}}$ too small
1:2:2 square prism	1.255	0.540	$0.1773 \pm 0.0000$	$1695 \pm 1$	$1096 \pm 1$	$[p_{\text{em}}(\text{FIR})]_{\text{max}}$ too large
1:2:2 spheroid	1.461	0.498	$0.1691 \pm 0.0001$	$1641 \pm 2$	$1034 \pm 10$	$[p_{\text{em}}(\text{FIR})]_{\text{max}}$ too small

*a*  $\Phi_{\text{PSA}}$  and  $\sigma_p$  from Table 1.

*b* Maximum FIR polarization fraction (Eq. 28).

*c*  $(C_{\text{pol,PSA}}/V)/\Phi_{\text{PSA}}$  averaged over 10–11 $\mu\text{m}$  (see Eq. 33).

*d* Silicate feature (see Eq. 35).

From Figures 9b and 9d (or Table 1), we see that 13 of the shapes considered here – 8 of the flattened shapes, and 5 of the elongated shapes – have  $\Phi_{\text{PSA}} > 0.7$ , and are therefore allowed by the *strength* of starlight polarization. Figures 10a,b show how  $\Phi_{\text{PSA}}$  depends on axial ratio and asymmetry parameter  $\mathcal{A}$ . Asymmetry parameter  $\mathcal{A}$  appears to be the better predictor of  $\Phi_{\text{PSA}}$ . In order to produce sufficient starlight polarization, flattened shapes ( $\mathcal{S} < 1$ ) should have  $\mathcal{A} \gtrsim 1.35$ , and elongated shapes ( $\mathcal{S} > 1$ ) should have  $\mathcal{A} \gtrsim 1.7$ .

Seven of the 20 considered shapes have  $\Phi_{\text{PSA}}$  that is too small, and therefore are ruled out by Equation (26). The low values of  $\Phi_{\text{PSA}}$  imply that such shapes cannot contribute substantially to the interstellar extinction.

In addition to satisfying (26), acceptable shapes must have  $\sigma_p < 0.60$  in order to reproduce the average Serkowski law (10) with  $K \approx 0.87$ . Of the 20 shapes studied, only 11 (see Table 2) are compatible with the Serkowski law (10) with the strength described by (16).

Recent work (Angarita et al. 2023) finds  $[p_{\text{max}}/E(B - V)]_{\text{max}} = 0.158_{-0.009}^{+0.013} \text{ mag}^{-1}$ , i.e., 22% more polarization per unit reddening than the value  $0.13 \text{ mag}^{-1}$  (Panopoulou et al. 2019; Planck Collaboration et al. 2020) adopted in the present study. If the larger value were to be adopted, then the minimum  $\Phi_{\text{PSA}}$  would increase from 0.70 (Eq. 26) to 0.85, ruling out some of the grain shapes (e.g. 2:1:1 spheroid, or 5:7:7 spheroid) which are allowed by  $\Phi_{\text{PSA}} > 0.7$ . Further observational work to better establish  $[p_{\text{max}}/E(B - V)]_{\text{max}}$  is needed.

### 10.2. Constraints from FIR and Submm Polarization

The thermal emission from aligned grains is polarized. The grains are in the Rayleigh limit  $a \ll \lambda$ , with  $Q_{\text{ext}} \approx Q_{\text{abs}}$ . The fractional polarization of the thermal emission is maximized if  $\mathbf{B}_0$  is in the plane of the sky, with

$$[p_{\text{em}}(\lambda)]_{\text{max}} = \frac{\langle f_{\text{align}} \rangle Q_{\text{pol,PSA}}(\lambda)}{\langle f_{\text{align}} \rangle Q_{\text{ext,PSA}}(\lambda) + (1 - \langle f_{\text{align}} \rangle) Q_{\text{ext,ran}}(\lambda)} . \quad (27)$$

Combining this with (24) and the condition  $\langle f_{\text{align}} \rangle < 0.7$  we obtain the predicted maximum polarization of thermal emission:

$$[p_{\text{em}}(\lambda)]_{\text{max}} = \frac{Q_{\text{pol,PSA}}(\lambda)}{Q_{\text{ext,PSA}}(\lambda) + \left[ \max\left(\frac{\Phi_{\text{PSA}}}{0.49}, \frac{1}{0.7}\right) - 1 \right] Q_{\text{ext,ran}}(\lambda)} , \quad (28)$$

plotted in Figure 11 for the 11 shapes with  $\Phi_{\text{PSA}} > 0.7$  and  $\sigma_p < 0.6$ . For all shapes, it is evident from Figure 11 that  $[p_{\text{em}}(\lambda)] \rightarrow [p_{\text{em}}(\text{FIR})]_{\text{max}} = \text{const}$  for  $\lambda \gtrsim 50 \mu\text{m}$ . Thus we can compare the predicted  $[p_{\text{em}}(100 \mu\text{m})]_{\text{max}}$  to the maximum polarization fraction at  $850 \mu\text{m}$  determined by Planck Collaboration et al. (2020):  $[p_{\text{em}}(850 \mu\text{m})]_{\text{max}} \approx 0.220_{-0.014}^{+0.035}$ , shown as the green shaded zone in Figure 11.

Five shapes appear to be consistent with both starlight polarization *and* the Planck polarization constraint: 5:7:7 (oblate) and 2:1:1 (prolate) spheroids<sup>5</sup>; 10:13:15 and 3:4:5 triaxial ellipsoids; and 5:2:2 square prisms.

Some of the other shapes fall below or above the Planck constraints:

**1:2:2 Oblate Spheroid:** Using the “oblate” dielectric function from Figure 2, this shape *underpredicts* the Planck fractional polarization, as previously found by Draine & Hensley (2021b). Thus this shape is ruled out, despite being compatible with the starlight polarization (see Table 2).

<sup>5</sup> Draine & Hensley (2021b) (DH21b) also found that 5:7:7 spheroids with porosity  $\mathcal{P}_{\text{micro}} = 0.2$  were viable, but concluded that 2:1:1 spheroids produced too much submm polarized emission per unit optical polarization. The slightly different conclusion of the present study is attributable to different choices of observational constraints. DH21b used the Planck determination of  $850 \mu\text{m}$  polarized intensity per unit visual polarization in diffuse clouds (Planck Collaboration et al. 2020), which requires an assumed grain temperature. Here we instead use the Planck Collaboration et al. (2020) estimates of the peak fractional polarization at  $850 \mu\text{m}$ , which does not require an assumed temperature, but does require accurate removal of unpolarized extragalactic backgrounds by the *Planck* team.

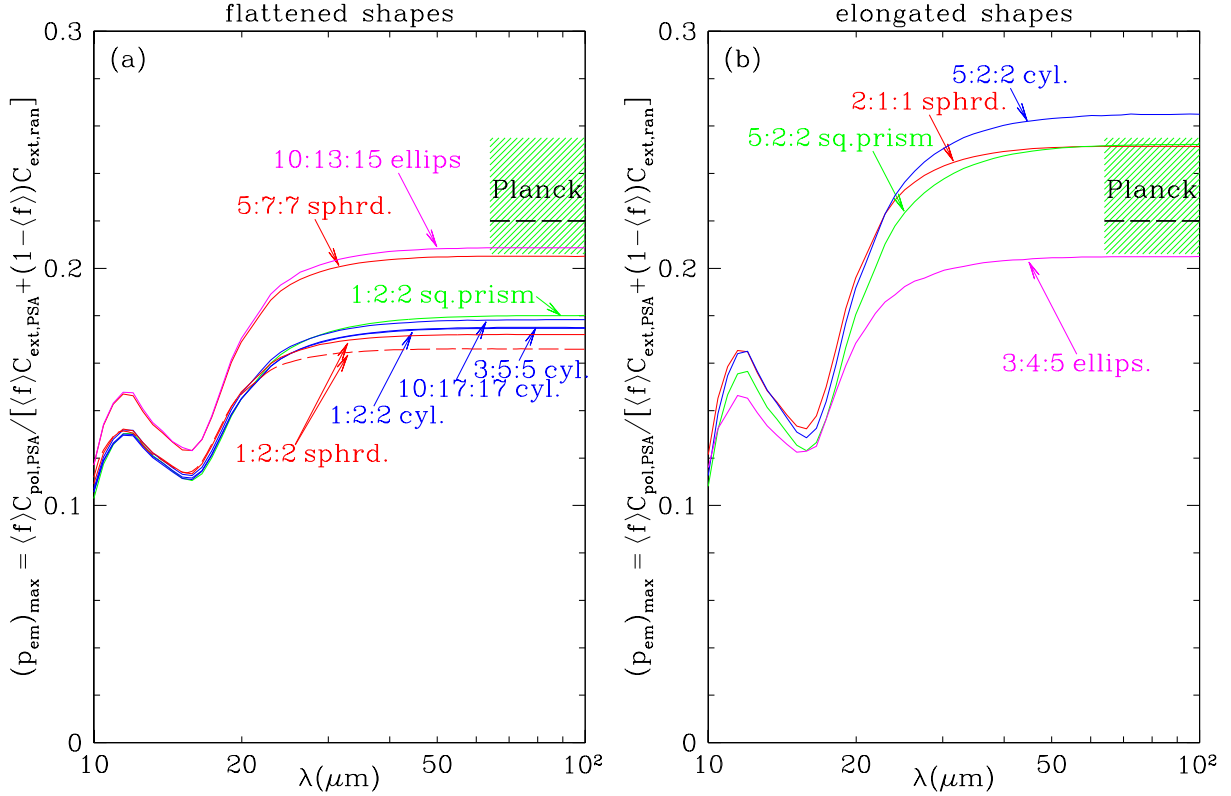


**Figure 11.** The maximum fractional polarization  $(p_{\text{em}})_{\text{max}}$  for thermal emission as a function of  $\lambda$  for (a) flattened shapes and (b) elongated shapes. Results are shown for  $a_{\text{eff}} = 0.2\mu\text{m}$ , but  $C_{\text{pol,PSA}}/V$ ,  $C_{\text{ext,PSA}}/V$ , and  $\Phi_{\text{PSA}}$  are essentially independent of  $a_{\text{eff}}$  for the grain sizes of interest (see Figs. 6, 7 and 9), and therefore so is  $(C_{\text{pol,PSA}}/C_{\text{ext,PSA}})/\Phi_{\text{PSA}}$ . The green shaded zone shows the range  $(p_{\text{em}})_{\text{max}} = 0.220^{+0.035}_{-0.014}$  allowed by Planck Collaboration et al. (2020). (a) Results for the “oblate” dielectric function in Fig. 2, except for the broken curve, calculated for the 1:2:2 spheroid using a self-consistent dielectric function (see text) – the reduction in FIR polarization is small. (b) Results for the “prolate” dielectric function in Fig. 2.

For the “oblate” dielectric function used here, the FIR-submm opacity calculated for the 1:2:2 spheroid is too large by  $\sim 20\%$  (see Figure 19a), which raises concern about the calculated fractional polarization. A dielectric function consistent with the observed FIR-submm opacity reduces  $\epsilon_2$  at long wavelengths (to lower the opacity), which reduces  $\epsilon_1$  at long wavelengths, resulting in a *reduction* in the fractional polarization of the submm emission relative to what was calculated using the “oblate” dielectric function from Figure 2. For the 1:2:2 spheroid, a self-consistent  $\epsilon(\lambda)$  was obtained by Draine & Hensley (2021b). The polarization calculated using this  $\epsilon(\lambda)$  is shown by the dashed curve in Figure 11a:  $[p_{\text{em}}(100\mu\text{m})]_{\text{max}}$  drops, but only slightly, from 17.1% to 16.6%.

**Flattened Cylinders:** The 10:17:17, 3:5:5, and 1:2:2 flattened cylinders all *underpredict* the Planck fractional polarization, and therefore are ruled out. We note that with the adopted dielectric function, these shapes have a FIR-submm opacity that is too large by 22–30% (see Figure 19). As discussed above, a self-consistent calculation for these shapes would *further* reduce the submm fractional polarization. Thus these shapes are ruled out, despite being compatible with the starlight polarization ( $\Phi_{\text{PSA}} > 0.7$  and  $\sigma_p < 0.6$ : see Table 2).

**5:2:2 Elongated Cylinder:** This shape *overpredicts* the submm fractional polarization. With the adopted dielectric functions, this shape also overpredicts the FIR opacity (see Figure 19). As discussed above, a self-consistent  $\epsilon(\lambda)$  would lead to a small *reduction* in the the polarization fraction at long wavelengths, but we expect the change to be small, as found for the 1:2:2 oblate spheroid.

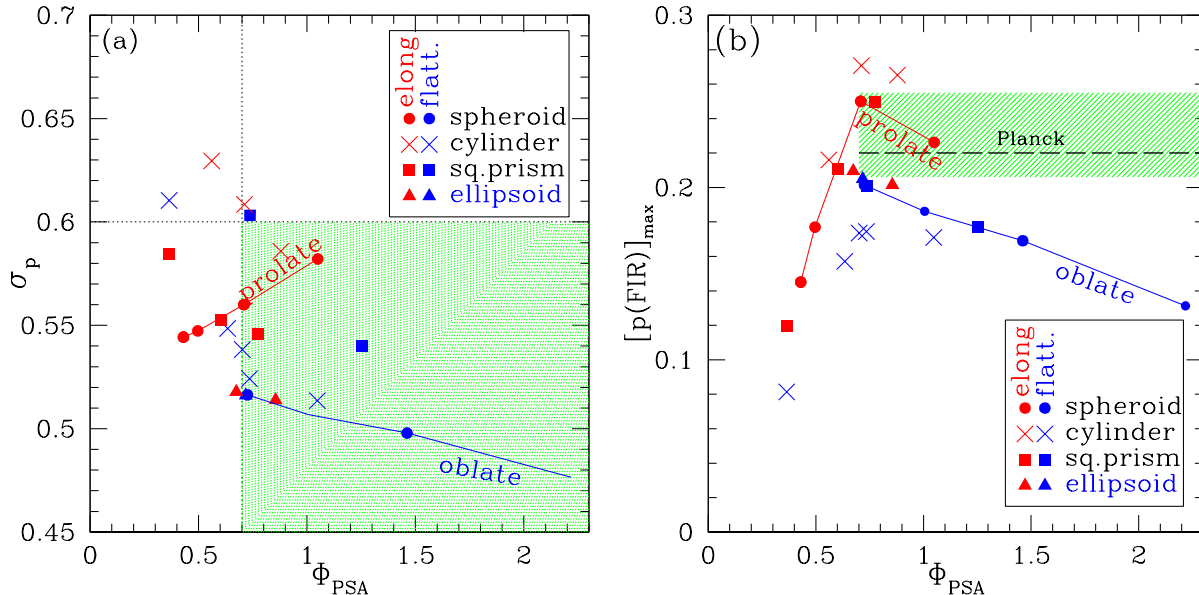


**Figure 12.** (a) Polarization profile width parameter  $\sigma_p$  vs. starlight polarization efficiency integral  $\Phi_{\text{PSA}}$  for different shapes, for  $a_{\text{eff}}$  values such that  $\lambda_p = 0.567\mu\text{m}$ . (b) Maximum FIR-submm polarization (Eq. 28) vs.  $\Phi_{\text{PSA}}$ . Symbols show the 20 shapes studied here using the DDA. Solid curves show results for prolate spheroids with axial ratios 1.5 – 3, and oblate spheroids with axial ratios 1.4 – 3.

For simplicity, the present discussion has presumed that all grains have the same shape. However, a mixture of shapes including some with  $[p_{\text{em}}]_{\text{max}} < 0.206$  and some with  $[p_{\text{em}}]_{\text{max}} > 0.255$  could collectively satisfy the *Planck* constraint  $[p_{\text{em}}]_{\text{max}} = 0.220^{+0.035}_{-0.014}$ .

### 10.3. On the Utility of Spheroids for Modeling Polarization

For the first time, we have studied the polarization properties of finite nonspheroidal grain shapes over a wide range of wavelengths.<sup>6</sup> Cross sections were calculated for a variety of convex shapes, both flattened and elongated, from the FUV ( $\lambda = 0.1\mu\text{m}$ ) to the FIR ( $\lambda = 100\mu\text{m}$ ).

Some grain geometries can be ruled out, because they are unable to generate sufficient starlight polarization (e.g., 3:2:2 spheroid), because they produce a polarization profile that is broader than observed (e.g., 2:3:3 square prism), or because they overpredict (e.g., 5:2:2 cylinder) or underpredict (e.g., 3:5:5 cylinder) the submm polarization fraction. However, some of the considered shapes remain viable.

For a given dielectric function  $\epsilon(\lambda)$ , we see from Figure 6 that different shapes with the same  $a_{\text{eff}}$  have similar (although not identical) extinction cross sections  $C_{\text{ran}}(\lambda)$ . The polarization cross sections  $C_{\text{pol,PSA}}(\lambda)$  exhibit more shape-to-shape variation (see Figure 7).

Figure 12a shows  $\Phi_{\text{PSA}}$  and  $\sigma_p$  for the twenty shapes studied; the allowed region ( $\Phi_{\text{PSA}} > 0.7$ ,  $\sigma_p < 0.6$ ) is shaded green. For each shape (see Table 1)  $a_{\text{eff}}$  is taken to be such that  $\lambda_p = 0.567\mu\text{m}$  as in the observed starlight polarization. Figure 12b shows the maximum FIR-submm polarization vs.  $\Phi_{\text{PSA}}$  for the twenty convex shapes in this study. The allowed region  $\Phi_{\text{PSA}} > 0.7$  and  $[p(\text{FIR})]_{\text{max}} = 0.220^{+0.035}_{-0.014}$  (Planck Collaboration et al. 2020) is shaded green.

It is much easier to calculate absorption and scattering cross sections for spheroids than for any other finite nonspherical shape. In the Rayleigh limit  $\lambda \gg a_{\text{eff}}$ , exact results for spheroids are easily

<sup>6</sup> Hong & Greenberg (1980) and others used results for infinite cylinders to estimate cross sections for finite cylinders

evaluated. For larger  $a_{\text{eff}}/\lambda$ , methods based on spheroidal wave functions (Voshchinnikov & Farafonov 1993) are much faster than the DDA for comparable levels of accuracy.

Prolate and oblate spheroids fall on the two tracks shown in Figure 12a. For axial ratios  $\leq 3$ , the spheroids have  $\sigma_p < 0.6$ , consistent with the observed polarization; prolate and oblate spheroids have  $\Phi_{\text{PSA}} > 0.7$  for axial ratio  $> 2$ , and  $> 1.4$ , respectively. Figure 12a shows that spheroids with suitable aspect ratios have  $(\Phi_{\text{PSA}}, \sigma_p)$  values passing through the allowed domain  $\Phi_{\text{PSA}} > 0.7$ ,  $\sigma_p < 0.6$ . Figure 12b shows the corresponding tracks in the  $\Phi_{\text{PSA}} - [p(\text{FIR})]_{\text{max}}$  plane, where we see that the only oblate shape that is allowed is  $b/a = 1.4$  (less flattened spheroids do not provide enough starlight polarization; more flattened spheroids do not have a large enough fractional polarization in the FIR). It appears that prolate shapes with axial ratios  $a/b \geq 2$  are allowed.

Spheroids cannot exactly reproduce the light scattering properties of specific nonspheroidal shapes, but can be used to approximate the scattering properties of submicron convex shapes that have  $\Phi_{\text{PSA}}$ ,  $\sigma_p$ , and  $[p(\text{FIR})]_{\text{max}}$  in the allowed range. While the detailed shape matters, spheroids continue to be useful to explore the effects of grain shape on polarized extinction and emission by interstellar grains.

#### 10.4. Which Axial Ratios are Favored?

Models seeking to reproduce the wavelength dependences of both extinction and polarization require that small ( $a_{\text{eff}} \lesssim 0.05\mu\text{m}$ ) grains are essentially nonpolarizing, while grains with  $a_{\text{eff}} \gtrsim 0.15\mu\text{m}$  are substantially polarizing (i.e., both significantly nonspherical *and* appreciably aligned), with  $f_{\text{align}}(a_{\text{eff}})\Phi_{\text{PSA}} \approx 0.7$  for  $a_{\text{eff}} \gtrsim 0.15\mu\text{m}$  (see, e.g., Figure 6 of Draine & Fraisse (2009) and Figure 1 of Hensley & Draine (2023)). As discussed above, in order to reproduce the highest values of  $p_{\text{max}}/E(B - V) \approx 0.13\text{mag}^{-1}$  observed for starlight polarization, the grains must have starlight polarization efficiency integral  $\Phi_{\text{PSA}} > 0.70$ . If a mixture of shapes is present, as seems likely, the  $a_{\text{eff}} \gtrsim 0.1\mu\text{m}$  grains must have mass-weighted  $\langle \Phi_{\text{PSA}} \rangle > 0.7$ .

The mechanisms responsible for alignment of interstellar grains remain incompletely understood, but it is plausible that above some critical size, starlight torques (Draine & Weingartner 1996, 1997) maintain a large fraction of the grains in suprathermal rotation, with high degrees of alignment resulting from a combination of starlight torques and paramagnetic or super-paramagnetic dissipation. If  $f_{\text{align}}(0.2\mu\text{m}) \approx 1$ , then  $\langle f_{\text{align}} \rangle \approx 0.7$ , and the observed starlight polarization can be accounted for by grains with  $\Phi_{\text{PSA}} \approx 0.49/\langle f_{\text{align}} \rangle \approx 0.7$ .

For this reason, it seems likely that the ‘‘typical’’ grains with  $a_{\text{eff}} \gtrsim 0.1\mu\text{m}$  will have shapes corresponding to  $\Phi_{\text{PSA}} \approx 0.7$ . From Figure 9 and Table 2 we see that this corresponds to an axial ratio  $\sim 1.4$  for oblate spheroids, or  $\sim 2$  for prolate spheroids. Other viable shapes (e.g., cylinders, square prisms, or trisphere) will have axial ratios  $\sim 1.5$  if flattened, or  $\sim 2$  if elongated. However, the more extreme flattened shapes (e.g., 1:2:2 spheroid) are unable to account for the fractional polarization observed by Planck at submm wavelengths (see Figure 11), and, therefore, cannot be dominant constituents.

#### 10.5. Polarization of the 10 $\mu\text{m}$ Silicate Feature

For  $\lambda \gtrsim 10\mu\text{m}$ , submicron grains are in the Rayleigh limit  $a_{\text{eff}} \ll \lambda$ , and  $C_{\text{pol}}/V$  is independent of  $a_{\text{eff}}$ . Initially unpolarized starlight will acquire a polarization

$$p(\lambda) = N_{\text{H}} V_{\text{gr}} \langle f_{\text{align}} \rangle \sin^2 \gamma \left[ \frac{C_{\text{pol,PSA}}(\lambda)}{V} \right], \quad (29)$$

provided  $p \lesssim 0.1$  so that the polarization is  $\sim$ linear in the optical depth. The observed starlight polarization integral (14) is

$$\Pi_{\text{obs}} \approx 1.23 \times 10^{-4} p_{\text{max}} \text{ cm} = N_{\text{H}} V_{\text{gr}} \langle f_{\text{align}} \rangle \sin^2 \gamma \Phi_{\text{PSA}}. \quad (30)$$



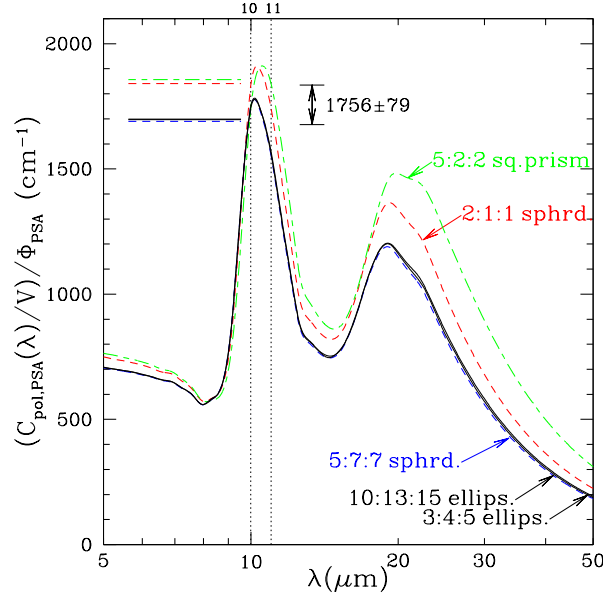


**Figure 13.**  $(C_{\text{pol,PSA}}/\lambda)/\Phi_{\text{PSA}}$  as a function of  $\lambda$  for 11 shapes allowed by starlight polarization (see text). Results are shown for  $a_{\text{eff}}$  values from Table 1, but  $(C_{\text{pol,PSA}}/\lambda)/\Phi_{\text{PSA}}$  is essentially independent of  $a_{\text{eff}}$  for  $\lambda > 5\mu\text{m}$  and the grain sizes of interest (see Figures 6 and 9). Flattened shapes (solid curves) generally have lower values of  $[C_{\text{pol,PSA}}(10 - 11\mu\text{m})/V]/\Phi_{\text{PSA}}$  than elongated shapes (broken curves).

Thus

$$N_{\text{H}}V_{\text{gr}}\langle f_{\text{align}} \rangle \sin^2 \gamma = \frac{1.23 \times 10^{-4} p_{\text{max}} \text{ cm}}{\Phi_{\text{PSA}}} . \quad (31)$$

Substituting (31) into (29) one obtains

$$\frac{p(\lambda)}{p_{\text{max}}} \approx 1.23 \times 10^{-4} \left[ \frac{C_{\text{pol,PSA}}(\lambda)/V}{\Phi_{\text{PSA}}} \right] \text{ cm} . \quad (32)$$

Figure 13 shows  $[C_{\text{pol,PSA}}/\lambda]/\Phi_{\text{PSA}}$  for  $\lambda \gtrsim 5\mu\text{m}$ . The grains are in the Rayleigh limit, hence  $C_{\text{pol,PSA}}/V$  is independent of  $a_{\text{eff}}$  (see Figure 7). We have already seen (Figure 9) that  $\Phi_{\text{PSA}}$  is nearly independent of  $a_{\text{eff}}$  for the grain sizes ( $0.10 - 0.30\mu\text{m}$ ) that dominate polarization. Thus  $[C_{\text{pol,PSA}}/\lambda]/\Phi_{\text{PSA}}$  in Figure 13 is nearly independent of  $a_{\text{eff}}$  for  $0.10 \lesssim a_{\text{eff}} \lesssim 0.30\mu\text{m}$ . Averaging over the  $10\mu\text{m}-11\mu\text{m}$  interval, the 5 shapes with  $\Phi_{\text{PSA}} > 0.7$ ,  $\sigma_p < 0.6$ , and  $[p_{\text{em}}(\text{FIR})]_{\text{max}} \in [0.20, 0.25]$  have

$$\overline{\frac{C_{\text{pol,PSA}}(10-11\mu\text{m})/V}{\Phi_{\text{PSA}}}} \approx 1756 \pm 79 \text{ cm}^{-1} . \quad (33)$$

Figure 13 shows that the flattened shapes have lower values of  $[C_{\text{pol,PSA}}(10-11\mu\text{m})/V]/\Phi_{\text{PSA}}$  compared to the elongated shapes. The polarization associated with the silicate feature itself can be characterized by the difference in mean polarization in the  $10-11\mu\text{m}$  and the  $8-9\mu\text{m}$  intervals:

$$\frac{\Delta C_{\text{pol,PSA}}(\text{sil.})}{V\Phi_{\text{PSA}}} \equiv \frac{\overline{C_{\text{pol,PSA}}(10-11\mu\text{m})} - \overline{C_{\text{pol,PSA}}(8-9\mu\text{m})}}{V\Phi_{\text{PSA}}} = 1153 \pm 93 \text{ cm}^{-1} . \quad (34)$$

The shapes in Figure 13 range from smooth spheroids to square solids (with sharp edges), and from flattened to elongated. The fact that *all* of the 11 convex shapes in Figure 13 make very similar

predictions for  $p(10 - 11\mu\text{m})/p_{\text{max}}$  suggests that other convex or nearly-convex shapes are likely to also fall in the range given by Eq. (33). From (32) and (33) one obtains

$$\left(\frac{\bar{p}(10-11\mu\text{m})}{p_{\text{max}}}\right)_{\text{theory}} \approx 0.216 \pm 0.010 \quad , \quad (35)$$

[in agreement with the value 0.22 found for spheroids by [Draine & Hensley \(2021b\)](#)] and

$$\left(\frac{\Delta p_{\text{sil.}}}{p_{\text{max}}}\right)_{\text{theory}} \approx 0.142 \pm 0.011 \quad . \quad (36)$$

The sightline to Cyg OB2-12 is the only sightline for which both optical and  $10\mu\text{m}$  polarization have been measured ([Telesco et al. 2022](#)), with  $p(10\mu\text{m}) = (1.24 \pm 0.28)\%$ ,  $\bar{p}(10-11\mu\text{m}) = (1.14 \pm 0.26)\%$  and  $\bar{p}(8-9\mu\text{m}) \approx (0.44 \pm 0.24)\%$ . With  $p_{\text{max}} = 0.0967 \pm 0.0010$  ([Whittet et al. 1992](#)), we have

$$\left(\frac{\bar{p}(10-11\mu\text{m})}{p_{\text{max}}}\right)_{\text{observed}} = 0.118 \pm 0.029 \quad , \quad (37)$$

a  $\sim 3.0\sigma$  discrepancy with the smallest value (0.206) allowed by Equation (35) for the 5 shapes considered here. Similarly,

$$\left(\frac{\Delta p_{\text{sil.}}}{p_{\text{max}}}\right)_{\text{observed}} = 0.072 \pm 0.025 \quad , \quad (38)$$

a  $2.4\sigma$  discrepancy with the smallest value (0.131) allowed by Eq. (36).

It is striking that *none* of the grain shapes considered here can account for the observed low values of  $p(10-11\mu\text{m})/p_{\text{max}}$  and  $\Delta p_{\text{sil.}}/p_{\text{max}}$  toward Cyg OB2-12. What does this tell us?

If the ratio  $\bar{p}(10 - 11\mu\text{m})/p_{\text{max}} = 0.118 \pm 0.029$  found by [Telesco et al. \(2022\)](#) toward Cyg OB2-12 is confirmed to apply to interstellar dust, then the following possibilities arise:

1. The actual grain shape may differ from the convex shapes considered here.
2. The adopted dielectric function may be incorrect.
3. The fundamental assumption of the astrodust model – that extinction and polarization at both optical and infrared wavelengths is dominated by a single type of grain – may be incorrect.

We consider these in turn:

#### 10.5.1. Grain Shape?

None of the convex shapes studied in this paper can reproduce the low value of  $C_{\text{pol}}(10\mu\text{m})/p_{\text{max}}$  observed toward Cyg OB2-12, but one can ask whether non-convex shapes might be able to. Paper II examines a number of very different, and very non-convex, shapes: coagulates. None of the coagulates studied in Paper II polarize strongly enough to account for the observed starlight polarization, and thus cannot explain the  $10\mu\text{m}$  polarization. Given the wide range of shapes considered here and in Paper II, it seems unlikely that merely changing the grain shape can resolve the discrepancy between predicted and observed values of  $\bar{p}(10 - 11\mu\text{m})/p_{\text{max}}$ .

### 10.5.2. Dielectric Function?

The predicted  $10\mu\text{m}$  polarization for “astrodust” was based on the dielectric function derived by DH21a from the infrared extinction law determined by Hensley & Draine (2020) for the sightline to Cyg OB2-12. The excess extinction  $\Delta\tau_{\text{sil}} \equiv \tau(9.7\mu\text{m}) - \tau(8\mu\text{m})$  in the  $10\mu\text{m}$  silicate feature can be reliably determined from the observed spectrum of Cyg OB2-12 (Hensley & Draine 2020). However, the underlying continuum extinction in the  $5\text{--}8\mu\text{m}$  region is controversial, requiring both accurate absolute photometry and an accurate estimate for the unobscured stellar flux. A 20% increase in the calibration of the Spitzer IR Spectrograph (Houck et al. 2004) (or a 20% decrease in the model for the flux from the photosphere + stellar wind at  $8\mu\text{m}$ ) would result in a factor of  $\sim 2$  reduction in the estimate for  $\tau(8\mu\text{m})$  toward Cyg OB2-12. The dielectric function used here predicts that  $\sim 30\%$  of the polarization at  $10\mu\text{m}$  arises from the underlying “continuum” opacity (i.e.,  $C_{\text{pol,PSA}}(8\mu\text{m}) \approx 0.30C_{\text{pol,PSA}}(10\mu\text{m})$  in Figure 13).

A recent study by Gordon et al. (2021) estimated the  $5\text{--}8\mu\text{m}$  extinction to be significantly lower than found by Hensley & Draine (2020). If the dielectric function used by the astrodust model were to be revised to be consistent with the extinction found by Gordon et al. (2021), the predicted polarization at  $10\mu\text{m}$  would be reduced.

Because the physics is intrinsically nonlinear,<sup>7</sup> recalculation of  $p(10\mu\text{m})/p_{\text{max}}$  requires a new self-consistent dielectric function, which will be the subject of future work. However, a rough estimate can be made by assuming the polarization to simply scale with the extinction. If the  $8\mu\text{m}$  extinction  $\tau(8\mu\text{m})$  were to be reduced by 50% (say), with the feature strength  $\Delta\tau_{\text{sil}} \equiv \tau(9.7\mu\text{m}) - \tau(8\mu\text{m})$  unchanged, the resulting  $p(10\mu\text{m})/p_{\text{max}}$  might be reduced by  $\sim 0.30 \times 50\% \approx 15\%$ , so that the predicted  $p(10\mu\text{m}) \approx 0.85 \times 0.022 = 0.018$ . The discrepancy with the observed value  $0.0124 \pm 0.0028$ , would become  $\sim 2\sigma$  – still appreciable. Future work will derive a new dielectric function consistent with the Gordon et al. (2021) extinction curve, but, based on the present discussion, this does not seem likely to bring the model into agreement with the Telesco et al. (2022) result for  $p(10\mu\text{m})/p_{\text{max}}$ .

### 10.5.3. The Astroduct Model?

The astroduct model (Hensley & Draine 2023) postulates that most of the interstellar grain mass is provided by grains with a single composition, incorporating both silicate and non-silicate material in the same particles. As we have seen above, the model prediction for  $p(10\mu\text{m})/p_{\text{max}}$  appears to be inconsistent with the measurement by Telesco et al. (2022) of  $p(10\mu\text{m})/p_{\text{max}}$  toward Cyg OB2-12.

It is not clear how the model could be modified to accommodate the measured value of  $p(10\mu\text{m})/p_{\text{max}}$ . One might try to concentrate the silicate material in grains that are less aspherical, or less well aligned, but the high ratio  $[p_{\text{max}}/E(B - V)]_{\text{max}} = 0.13$  for starlight polarization (Panopoulou et al. 2019) as well as submm polarization fractions exceeding 20% (Planck Collaboration et al. 2020) require that a large fraction of the dust grains be both substantially nonspherical and highly aligned. Given that the silicate material must account for a major fraction of the dust mass in the diffuse ISM, it is hard to see how a substantial fraction of the silicate mass could be sequestered in grains that are relatively inefficient polarizers. In addition, if the silicate and non-silicate materials are in separate grain populations (with different opacities, shapes, and degrees of alignment), the polarization fraction at FIR and submm wavelengths will be wavelength-dependent, as in the models of Draine & Fraisie (2009), whereas the observed polarization fraction appears to be nearly independent of wavelength (see Hensley & Draine 2021).

The  $10\mu\text{m}$  polarization is evidently a powerful test of interstellar grain models. Further measurements of  $10\mu\text{m}$  polarization (with CanariCam or other instruments) toward Cyg OB2-12 and other sightlines, and additional studies of the  $4\text{--}8\mu\text{m}$  extinction (with JWST) will be of great value.

<sup>7</sup>  $p(10\mu\text{m})$  depends nonlinearly on both the real and imaginary parts of the dielectric function.

#### 10.5.4. *Is Cyg OB2-12 A Suitable Target?*

Studies of the polarizing properties of the dust toward Cyg OB2-12 have assumed that the light from Cyg OB2-12 is unpolarized, so that the observed polarization is entirely the result of extinction by aligned dust grains along the line-of-sight. Is this correct?

Cyg OB2-12 is a very unusual star: a blue hypergiant, classified as B5Ia<sup>+</sup> by Humphreys (1978), and as B3Iae by Kiminki et al. (2007). At an assumed distance  $D = 1.75$  kpc, it is one of the most luminous stars in the Galaxy, with luminosity  $L = 1.4 \times 10^6 L_\odot$  (Clark et al. 2012; Hensley & Draine 2020). Cyg OB2-12 varies in brightness ( $\Delta B \approx 0.3$  mag; Gottlieb & Liller 1978; Laur et al. 2012; Salas et al. 2015), and in spectrum, with spectral class changing from B3 to B8 in 12 months (Kiminki et al. 2007). The stellar wind produces absorption and emission features (Clark et al. 2012; Hensley & Draine 2020). The ionized wind is detected at cm wavelengths, showing unexpected variability at 21 cm (Morford et al. 2016).

Cyg OB2-12 appears to be a member of a triple system, with a companion at projected separation  $\sim 100$  au, and a second companion at projected separation  $\sim 2000$  au (Caballero-Nieves et al. 2014; Maryeva et al. 2016). Klochkova et al. (2022) report radial velocity variations of amplitude  $\sim 8$  km s<sup>-1</sup>; if periodic, the period must be  $\lesssim 2$  yr. Oskinova et al. (2017) argue that Cyg OB2-12 is a colliding-wind binary.

The polarization position angle PA is wavelength-dependent. Pre-2015 observations were consistent with

$$PA \approx 115^\circ + 1.7^\circ(\mu\text{m}/\lambda) \text{ for } 0.44\mu\text{m} < \lambda < 2.2\mu\text{m} \quad , \quad (39)$$

(see Figure 4 of Whittet 2015) which can be explained by a model with two separate dust layers along the line of sight, with different alignment directions (PA=56° and PA=125°), and different wavelength dependence for the polarization (McMillan & Tapia 1977; Whittet 2015). Such a two-layer model is consistent with the observed circular polarization (Martin & Angel 1976). However, Telesco et al. (2022) observe PA = 126° at  $\lambda = 10\mu\text{m}$ , inconsistent with (39), and inconsistent with the two-layer model of Whittet (2015), unless the “foreground” dust layer (assumed to contribute  $A_V = 3.6$  mag and  $p_V = 0.0335$ ) for some reason contributes zero polarization at  $10\mu\text{m}$ .

Furthermore, there are indications that the linear polarization may be time-variable. In the J band, Dyck & Jones (1978) found  $p(\text{J}) = 0.0331 \pm 0.0017$ , Wilking et al. (1980) found  $p(\text{J}) = 0.0410 \pm 0.0013$ , and Bailey & Hough (1982) found  $p(\text{J}) = 0.0370 \pm 0.0008$ . In the K band, Wilking et al. (1980) found  $p(\text{K}) = 0.0133 \pm 0.0005$ , and Bailey & Hough (1982) found  $p(\text{K}) = 0.0113 \pm 0.0003$ . Blinov et al. (2023) report substantial variations of  $U/I$  and  $Q/I$  over 2400 days of observations.

If the polarization of Cyg OB2-12 is actually variable on a  $\sim 1$  yr time scale, the variations must be due to changing polarization of the star itself, in which case Cyg OB2-12 becomes much less useful for studying polarization by interstellar dust, and Eqs. (37, 38) need not apply to interstellar dust. Intrinsic stellar polarization in Cyg OB2-12 could arise from electron scattering in the ionized outflow if it departs from spherical symmetry.<sup>8</sup> It is important to remeasure both optical and mid-IR polarization toward Cyg OB2-12, to test for time-dependence. If Cyg OB2-12 has intrinsic polarization, there will be a strong need for measurements of both optical and  $10\mu\text{m}$  polarization for other sightlines.

#### 10.6. *Polarization of the 3.4 $\mu\text{m}$ Feature*

The “astrodust” dielectric function used here includes an absorption feature at  $3.4\mu\text{m}$  arising from the C-H stretching mode in aliphatic hydrocarbons assumed to be present in “astrodust”. DH21a noted that this model predicts a polarization feature at  $3.4\mu\text{m}$  that exceeds observational upper limits. DH21a proposed that if the  $3.4\mu\text{m}$  absorbers are present only near the grain surface, rather

<sup>8</sup> The Cyg OB2-12 wind model (Clark et al. 2012; Hensley & Draine 2020) has  $\sigma_T \int_{R_*}^{\infty} n_e(r) dr = 0.43$ , where  $\sigma_T$  is the Thompson scattering cross section. Thus a large fraction of the photons emitted by the photosphere will be scattered in the wind, leading to net polarization if the wind is asymmetric.

than throughout the grain volume, the  $3.4\mu\text{m}$  polarization will be weakened because a larger fraction of the  $3.4\mu\text{m}$  absorption will then be contributed by minimally-aligned  $a \lesssim 0.1\mu\text{m}$  grains. DH21a estimated that if the  $3.4\mu\text{m}$  absorbers are located only in a surface layer of thickness  $\sim 0.010\mu\text{m}$ , the predicted polarization in the  $3.4\mu\text{m}$  feature becomes comparable to current upper limits.

If  $3.4\mu\text{m}$  C-H absorption is concentrated near the grain surface, the astroduct model should be modified to allow for spatial variation in the dielectric function within the grain, at least near  $3.4\mu\text{m}$ ; elaboration along these lines will be considered in future work. Polarization in the  $3.4\mu\text{m}$  feature can be weakened but not eliminated: further improvements in mid-IR spectropolarimetry should detect polarization of the  $3.4\mu\text{m}$  feature.

Just as for the silicate feature, polarization of the  $3.4\mu\text{m}$  feature relative to optical polarization (not shown here) is relatively insensitive to shape for the compact convex shapes considered here.

## 11. SUMMARY

The principal results are as follows:

1. The starlight polarization efficiency integral  $\Phi_{\text{PSA}}$  and the polarization width  $\sigma_p$  are integral properties of grains that can be used to test grain candidates. Interstellar grains should have  $\Phi_{\text{PSA}} > 0.7$  and  $\sigma_p < 0.6$ .
2. An additional test is provided by the submillimeter polarization: some shapes predict too much submm polarization (relative to optical polarization), while others predict too little.
3. Twenty convex shapes were studied using the DDA: spheroids, cylinders, square prisms, and triaxial ellipsoids. Only 11 of these shapes have  $\Phi_{\text{PSA}}(a_{\text{eff}}) > 0.7$ , and  $\sigma_p < 0.6$ , as required to reproduce the polarization of starlight. Only 5 of the 20 shapes studied are compatible with both starlight polarization *and* submm polarization (see Table 1, Table 2, and Figure 12).
4. While the extinction and polarization cross sections per volume  $C_{\text{ran}}(\lambda)/V$  and  $C_{\text{pol}}(\lambda)/V$  vary from shape to shape, shapes that are consistent with observational constraints can be well-approximated by spheroids with appropriate axis ratios.
5. All shapes have similar  $[C_{\text{pol,PSA}}(\lambda)/V]/\Phi_{\text{PSA}}$  at mid-infrared wavelengths  $8\text{--}15\mu\text{m}$ . The different shapes therefore predict similar ratios  $p(10\mu\text{m})/p_{\text{max}}$ , where  $p_{\text{max}}$  is the peak starlight polarization.
6. The discrepancy between the predicted (Draine & Hensley 2021b) and observed (Telesco et al. 2022)  $10\mu\text{m}$  polarization of Cyg OB2-12 does not seem likely to be resolved by varying the assumed grain shape.
7. Cyg OB2-12 may be intrinsically polarized, which would call into question its use to study interstellar polarization in the infrared. It is important to measure  $p(10\mu\text{m})/p_{\text{max}}$  on other sightlines.

<sup>1</sup> This work was supported in part by NSF grant AST-1908123. I thank C. Telesco and F. Varosi for  
<sup>2</sup> kindly providing machine-readable data for Cyg OB2-12, Robert Lupton for availability of the SM  
<sup>3</sup> package, and the anonymous referee for helpful comments.

## REFERENCES

- |   |  |
|---|--|
| <p>Andersson, B.-G., Lazarian, A., &amp; Vaillancourt, J. E. 2015, ARA&amp;A, 53, 501,<br/>doi: <a href="https://doi.org/10.1146/annurev-astro-082214-122414">10.1146/annurev-astro-082214-122414</a></p> | <p>Angarita, Y., Versteeg, M. J. F., Haverkorn, M., et al. 2023, arXiv e-prints, arXiv:2306.07016,<br/><a href="https://arxiv.org/abs/2306.07016">https://arxiv.org/abs/2306.07016</a></p> |
|---|--|



- Ashton, P. C., Ade, P. A. R., Angilè, F. E., et al. 2018, *ApJ*, 857, 10, doi: [10.3847/1538-4357/aab3ca](https://doi.org/10.3847/1538-4357/aab3ca)
- Bailey, J., & Hough, J. H. 1982, *PASP*, 94, 618, doi: [10.1086/131032](https://doi.org/10.1086/131032)
- Blinov, D., Maharana, S., Bouzelou, F., et al. 2023, arXiv e-prints, arXiv:2307.06151, doi: [10.48550/arXiv.2307.06151](https://doi.org/10.48550/arXiv.2307.06151)
- Bohren, C. F., & Huffman, D. R. 1983, *Absorption and Scattering of Light by Small Particles* (New York: Wiley)
- Caballero-Nieves, S. M., Nelan, E. P., Gies, D. R., et al. 2014, *AJ*, 147, 40, doi: [10.1088/0004-6256/147/2/40](https://doi.org/10.1088/0004-6256/147/2/40)
- Clark, J. S., Najarro, F., Negueruela, I., et al. 2012, *A&A*, 541, A145, doi: [10.1051/0004-6361/201117472](https://doi.org/10.1051/0004-6361/201117472)
- Collinge, M. J., & Draine, B. T. 2004, *J. Opt. Soc. Am. A*, 21, 2023, doi: [10.1364/JOSAA.21.002023](https://doi.org/10.1364/JOSAA.21.002023)
- Davis, L. J., & Greenstein, J. L. 1951, *ApJ*, 114, 206, doi: [10.1086/145464](https://doi.org/10.1086/145464)
- Draine, B. T. 1988, *ApJ*, 333, 848, doi: [10.1086/166795](https://doi.org/10.1086/166795)
- Draine, B. T., & Flatau, P. J. 1994, *J. Opt. Soc. Am. A*, 11, 1491, doi: [10.1364/JOSAA.11.001491](https://doi.org/10.1364/JOSAA.11.001491)
- Draine, B. T., & Fraisse, A. A. 2009, *ApJ*, 696, 1, doi: [10.1088/0004-637X/696/1/1](https://doi.org/10.1088/0004-637X/696/1/1)
- Draine, B. T., & Goodman, J. 1993, *ApJ*, 405, 685, doi: [10.1086/172396](https://doi.org/10.1086/172396)
- Draine, B. T., & Hensley, B. S. 2021a, *ApJ*, 909, 94, doi: [10.3847/1538-4357/abd6c6](https://doi.org/10.3847/1538-4357/abd6c6)
- . 2021b, *ApJ*, 919, 65, doi: [10.3847/1538-4357/ac0050](https://doi.org/10.3847/1538-4357/ac0050)
- Draine, B. T., & Weingartner, J. C. 1996, *ApJ*, 470, 551, doi: [10.1086/177887](https://doi.org/10.1086/177887)
- . 1997, *ApJ*, 480, 633, doi: [10.1086/304008](https://doi.org/10.1086/304008)
- Dyck, H. M., & Jones, T. J. 1978, *AJ*, 83, 594, doi: [10.1086/112240](https://doi.org/10.1086/112240)
- Goodman, J., Draine, B. T., & Flatau, P. J. 1991, *Optics Letters*, 16, 1198, doi: [10.1364/OL.16.001198](https://doi.org/10.1364/OL.16.001198)
- Gordon, K. D., Misselt, K. A., Bouwman, J., et al. 2021, *ApJ*, 916, 33, doi: [10.3847/1538-4357/ac00b7](https://doi.org/10.3847/1538-4357/ac00b7)
- Gottlieb, E. W., & Liller, W. 1978, *ApJ*, 225, 488, doi: [10.1086/156509](https://doi.org/10.1086/156509)
- Guillet, V., Fanciullo, L., Verstraete, L., et al. 2018, *A&A*, 610, A16, doi: [10.1051/0004-6361/201630271](https://doi.org/10.1051/0004-6361/201630271)
- Gutkowicz-Krusin, D., & Draine, B. T. 2004, ArXiv e-prints, <http://arXiv.org/abs/astro-ph/0403082>
- Hall, J. S. 1949, *Science*, 109, 166, doi: [10.1126/science.109.2825.166](https://doi.org/10.1126/science.109.2825.166)
- Hensley, B. S., & Draine, B. T. 2020, *ApJ*, 895, 38, doi: [10.3847/1538-4357/ab8cc3](https://doi.org/10.3847/1538-4357/ab8cc3)
- . 2021, *ApJ*, 906, 73, doi: [10.3847/1538-4357/abc8f1](https://doi.org/10.3847/1538-4357/abc8f1)
- . 2023, *ApJ*, 948, 55, doi: [10.3847/1538-4357/acc4c2](https://doi.org/10.3847/1538-4357/acc4c2)
- Hiltner, W. A. 1949, *Nature*, 163, 283, doi: [10.1038/163283a0](https://doi.org/10.1038/163283a0)
- Hong, S. S., & Greenberg, J. M. 1980, *A&A*, 88, 194
- Houck, J. R., Roellig, T. L., van Cleve, J., et al. 2004, *ApJS*, 154, 18, doi: [10.1086/423134](https://doi.org/10.1086/423134)
- Humphreys, R. M. 1978, *ApJS*, 38, 309, doi: [10.1086/190559](https://doi.org/10.1086/190559)
- Kim, S.-H., & Martin, P. G. 1995, *ApJ*, 444, 293, doi: [10.1086/175604](https://doi.org/10.1086/175604)
- Kiminki, D. C., Kobulnicky, H. A., Kinemuchi, K., et al. 2007, *ApJ*, 664, 1102, doi: [10.1086/513709](https://doi.org/10.1086/513709)
- Klochkova, V. G., Islientieva, E. S., & Panchuk, V. E. 2022, *Astronomy Reports*, 66, 998, doi: [10.1134/S1063772922110099](https://doi.org/10.1134/S1063772922110099)
- Laur, J., Tuvikene, T., Eenmäe, T., Kolka, I., & Leedjärv, L. 2012, *Baltic Astronomy*, 21, 531, doi: [10.1515/astro-2017-0409](https://doi.org/10.1515/astro-2017-0409)
- Lenz, D., Hensley, B. S., & Doré, O. 2017, *ApJ*, 846, 38, doi: [10.3847/1538-4357/aa84af](https://doi.org/10.3847/1538-4357/aa84af)
- Martin, P. G., & Angel, J. R. P. 1976, *ApJ*, 207, 126, doi: [10.1086/154476](https://doi.org/10.1086/154476)
- Martin, P. G., Clayton, G. C., & Wolff, M. J. 1999, *ApJ*, 510, 905, doi: [10.1086/306613](https://doi.org/10.1086/306613)
- Maryeva, O. V., Chentsov, E. L., Goranskij, V. P., et al. 2016, *MNRAS*, 458, 491, doi: [10.1093/mnras/stw385](https://doi.org/10.1093/mnras/stw385)
- Mathis, J. S., Ruml, W., & Nordsieck, K. H. 1977, *ApJ*, 217, 425
- McMillan, R. S., & Tapia, S. 1977, *ApJ*, 212, 714, doi: [10.1086/155096](https://doi.org/10.1086/155096)
- Morford, J. C., Fenech, D. M., Prinja, R. K., Blomme, R., & Yates, J. A. 2016, *MNRAS*, 463, 763, doi: [10.1093/mnras/stw1914](https://doi.org/10.1093/mnras/stw1914)



- Oskinova, L. M., Huenemoerder, D. P., Hamann, W.-R., et al. 2017, *ApJ*, 845, 39, doi: [10.3847/1538-4357/aa7e79](https://doi.org/10.3847/1538-4357/aa7e79)
- Panopoulou, G. V., Hensley, B. S., Skalidis, R., Blinov, D., & Tassis, K. 2019, *A&A*, 624, L8, doi: [10.1051/0004-6361/201935266](https://doi.org/10.1051/0004-6361/201935266)
- Planck Collaboration, Adam, R., Ade, P. A. R., et al. 2016, *A&A*, 594, A1, doi: [10.1051/0004-6361/201527101](https://doi.org/10.1051/0004-6361/201527101)
- Planck Collaboration, Aghanim, N., Akrami, Y., et al. 2020, *A&A*, 641, A12, doi: [10.1051/0004-6361/201833885](https://doi.org/10.1051/0004-6361/201833885)
- Purcell, E. M., & Pennypacker, C. R. 1973, *ApJ*, 186, 705, doi: [10.1086/152538](https://doi.org/10.1086/152538)
- Salas, J., Maíz Apellániz, J., & Barbá, R. H. 2015, in *Highlights of Spanish Astrophysics VIII*, 615–615, doi: [10.48550/arXiv.1410.6767](https://doi.org/10.48550/arXiv.1410.6767)
- Serkowski, K. 1973, in *Interstellar Dust and Related Topics*, ed. J. M. Greenberg & H. C. van de Hulst, Vol. 52, 145
- Serkowski, K., Mathewson, D. S., & Ford, V. L. 1975, *ApJ*, 196, 261, doi: [10.1086/153410](https://doi.org/10.1086/153410)
- Shen, Y., Draine, B. T., & Johnson, E. T. 2008, *ApJ*, 689, 260, doi: [10.1086/592765](https://doi.org/10.1086/592765)
- Siebenmorgen, R., Voshchinnikov, N. V., & Bagnulo, S. 2014, *A&A*, 561, A82, doi: [10.1051/0004-6361/201321716](https://doi.org/10.1051/0004-6361/201321716)
- Telesco, C. M., Varosi, F., Wright, C., et al. 2022, *ApJL*, 940, L26, doi: [10.3847/2041-8213/ac9b56](https://doi.org/10.3847/2041-8213/ac9b56)
- Voshchinnikov, N. V., & Farafonov, V. G. 1993, *Ap&SS*, 204, 19
- Whittet, D. C. B. 2015, *ApJ*, 811, 110, doi: [10.1088/0004-637X/811/2/110](https://doi.org/10.1088/0004-637X/811/2/110)
- . 2022, *Dust in the Galactic Environment (Third Edition)*, 2514-3433 (IOP Publishing), doi: [10.1088/2514-3433/ac7204](https://doi.org/10.1088/2514-3433/ac7204)
- Whittet, D. C. B., Martin, P. G., Hough, J. H., et al. 1992, *ApJ*, 386, 562, doi: [10.1086/171039](https://doi.org/10.1086/171039)
- Wilking, B. A., Lebofsky, M. J., Martin, P. G., Rieke, G. H., & Kemp, J. C. 1980, *ApJ*, 235, 905, doi: [10.1086/157694](https://doi.org/10.1086/157694)

## APPENDIX

## A. APPLYING THE DISCRETE DIPOLE APPROXIMATION

We seek to calculate scattering and absorption of monochromatic radiation by targets composed of material characterized by a complex dielectric function  $\epsilon(\lambda)$ . The discrete dipole approximation (DDA) consists of replacing the continuum target by an array of polarizable points (Purcell & Penny-packer 1973; Draine 1988; Draine & Flatau 1994), and solving the scattering problem for this array. The calculations are greatly accelerated by employing fast Fourier transforms (Goodman et al. 1991).

The dipoles are located on a cubic lattice with interdipole separation  $d$ . We employ the public domain code DDSCAT 7.3.3<sup>1</sup>. The DDSCAT error tolerance parameter is set to TOL= $1 \times 10^{-5}$ .

Accuracy of the DDA requires that the dipole array provide a good geometric approximation to the actual target, *and* that the dipole separation  $d$  be small enough that the phase shift between lattice sites be small. Draine & Flatau (1994) recommended

$$|m|kd \lesssim 0.5 \tag{A1}$$

which corresponds to a requirement on the number of dipoles:

$$N \gtrsim 8300|m|^3 \left(\frac{a_{\text{eff}}}{\lambda}\right)^3 . \tag{A2}$$

**Table 3.** Numbers of dipoles used

shape	$N_1$	$N_2$	$N_3$
5:7:7 cylinder	1538000	788480	404480
5:8:8 cylinder	1031360	433920	129120
5:7:7 spheroid	2199512	793312	336264
10:13:15 ellipsoid	1031224	306912	130162
3:5:5 cylinder	813888	241152	101180
10:17:17 cylinder	847584	491040	206685
2:3:3 square prism	1152000	589824	248832
1:2:2 cylinder	825088	374136	103296
1:2:2 spheroid	1082288	458136	136680
1:2:2 square prism	1048576	442368	131072
3:2:2 square prism	768000	324000	165888
3:2:2 spheroid	793152	407144	172640
4:5:6 ellipsoid	509216	295316	125206
3:4:5 ellipsoid	856744	439792	108120
5:3:3 cylinder	956400	488160	206280
2:1:1 square prism	524288	221184	65536
2:1:1 spheroid	769792	277888	117640
2:1:1 cylinder	1147680	413184	173769
5:2:2 square prism	933120	274680	81920
5:2:2 cylinder	730800	424200	216480

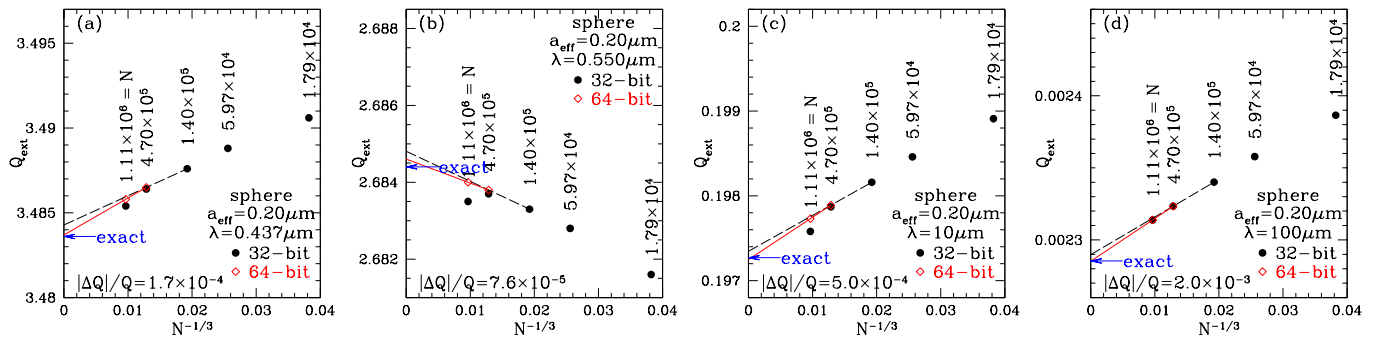


**Figure 14.** DDA calculations of  $Q_{\text{ext,ran}}$  for  $a = 0.10\mu\text{m}$  spheres as a function of  $N^{-1/3}$ , where  $N$  is the number of dipoles used to represent the sphere. The dielectric function in Figure 2 is employed. Results are shown for four wavelengths. In each case the exact result calculated with Mie theory is shown. Extrapolation using Equation (8) (solid and dashed lines) is seen to yield very accurate results.

At  $\lambda = 0.1\mu\text{m}$ , the astrodust dielectric function  $m = 1.41 + 0.70i$ . Eq. (A2) becomes

$$N(\lambda = 0.1\mu\text{m}) > 3.3 \times 10^4 \left( \frac{a_{\text{eff}}}{0.1\mu\text{m}} \right)^3. \quad (\text{A3})$$

For  $a_{\text{eff}} = 0.2\mu\text{m}$  this becomes  $N > 2.6 \times 10^5$ . For each of the 20 shapes considered here we repeat the DDA calculations for three values  $N_1 > N_2 > N_3$  (see Table 3) with  $N_1 > 5 \times 10^5$  for every shape to ensure accuracy. For cases with  $N > 5 \times 10^5$ , the DDSCAT calculations are carried out using 64-bit arithmetic to avoid round-off error. Parameter files (`ddscat.par`) as well as files specifying the dielectric functions used in the DDSCAT calculations are available online at [Replication Data for: Polarization and Grain Shape: Convex Shapes](#).

## B. ACCURACY OF THE DDA

### B.1. Spheres

To verify the accuracy of the DDA, we use the DDA to calculate scattering and absorption by spheres. As discussed in section 5.1, results calculated for two different numbers of dipoles  $N$  are used to extrapolate to  $N \rightarrow \infty$ , and compared with exact cross sections calculated using Mie theory. Figure 14 shows results for spheres with radii  $a = 0.2\mu\text{m}$  and 4 selected wavelengths, from the vacuum ultraviolet to the FIR. Extrapolation to  $N \rightarrow \infty$  gives results that are in excellent agreement with the exact solutions. In all 4 cases shown, the estimate  $\Delta Q/Q$  for the fractional uncertainty is seen to be very conservative: the actual errors in the extrapolated  $Q_{\text{ext}}$  are in all cases significantly smaller than  $|\Delta Q|$  from Equation (9).

### B.2. Cylinders and Square Prisms

In this section similar studies are carried out for cylinders and square prisms, to confirm that the behavior found for spheroids (see Figures 4 and 5) is general.

Figures 15 and 16 show  $Q_{\text{ext,ran}}$  vs.  $N^{-1/3}$  for 2:1:1 cylinders and 2:1:1 square prisms, both with  $a_{\text{eff}} = 0.2\mu\text{m}$ , at four selected wavelengths, just as for 2:1:1 spheroids in Figure 4. The 2:1:1 cylinder has a fractional uncertainty of 0.2% in  $Q_{\text{ext,ran}}$  at  $0.55\mu\text{m}$  (Figure 15b), and 0.5% at  $100\mu\text{m}$  (Figure 15d). these uncertainties are not large enough to alter any of the conclusions in this paper.

Figure 17 shows the fractional uncertainties in  $Q_{\text{ext,ran}}$  obtained from Equation (8) for 8 different convex shapes, 4 values of  $a_{\text{eff}}$ , and the full range of wavelengths  $\lambda$  from  $0.1\mu\text{m}$  to  $100\mu\text{m}$ . For the values of  $N$  used, the fractional errors in  $Q_{\text{ext,ran}}$  are generally quite small. For these convex shapes, the DDA gives results for  $Q_{\text{ext,ran}}$  with uncertainties well below 1%.

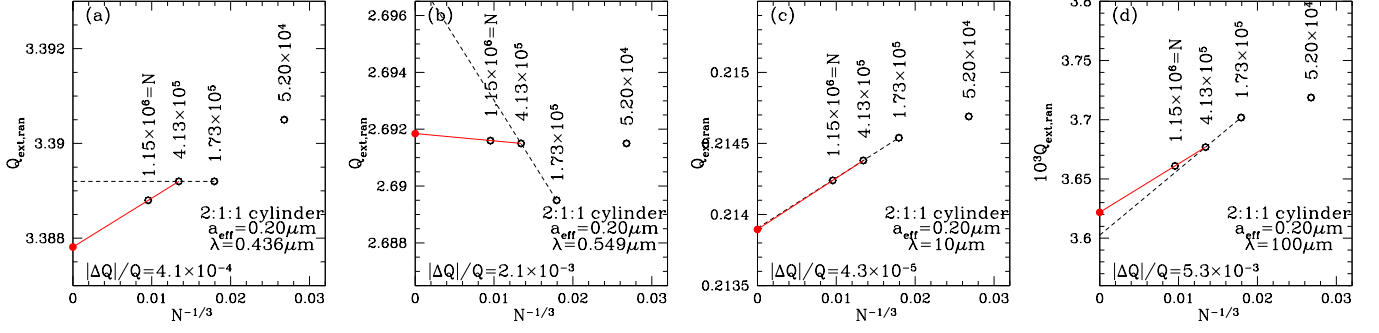


Figure 15. Similar to Figure 4, but showing  $Q_{\text{ext,ran}}$  for randomly-oriented 2:1 cylinders.

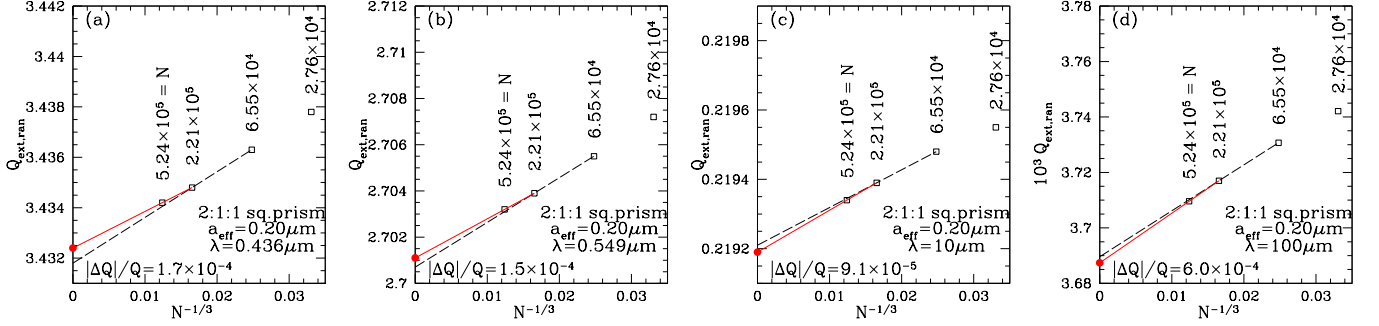


Figure 16. Similar to Figure 4, but showing  $Q_{\text{ext,ran}}$  for randomly-oriented 2:1:1 square prisms.

Polarization cross sections depend on differences of cross sections, and can be small or even negative at short wavelengths (see Figure 7). Thus the fractional error  $\Delta Q_{\text{pol,PSA}}/Q_{\text{pol,PSA}}$  can become large at short wavelengths, even though the absolute error in  $Q_{\text{pol,PSA}}$  may be small. Therefore we instead consider the ratio  $|\Delta Q_{\text{pol,PSA}}|/Q_{\text{ext,ran}}$ . Figure 18 shows  $|\Delta Q_{\text{pol,PSA}}|/Q_{\text{ext,ran}}$  for the eight shapes. For the  $N$  values used here, the uncertainties in  $Q_{\text{pol,PSA}}$  are generally well below 1% of  $Q_{\text{ext,ran}}$ .

The dependence of the extinction efficiency factor  $Q_{\text{ext}}(\Theta)$  and the polarization efficiency factor  $Q_{\text{pol}}(\Theta)$  on the orientation angle  $\Theta$  is shown in Figure 20 for  $a_{\text{eff}} = 0.2\mu\text{m}$  grains with the three different shapes. For the axisymmetric shapes considered here, the polarization efficiency  $Q_{\text{pol}} \rightarrow 0$  for  $\Theta \rightarrow 0$ , or  $\cos^2 \Theta \rightarrow 1$ . For elongated grains in the Rayleigh limit  $\lambda \gg a_{\text{eff}}$ ,  $Q_{\text{ext}}(\Theta)$  has a minimum at  $\Theta = 0$ , but at optical wavelengths this need not be the case; for the examples shown here,  $Q_{\text{ext}}$  is maximum for  $\Theta = 0$  for  $\lambda = 0.44\mu\text{m}$  and  $\lambda = 0.55\mu\text{m}$ .

### C. EFFECT OF SHAPE ON FIR OPACITY

To see how shape influences the FIR absorption, Figure 19 shows the ratio of the opacity of these different shapes at wavelength  $\lambda$  relative to the opacity for the 5:7:7 oblate spheroid:

$$R_{\text{ext,ran}}(\text{shape}, \lambda) \equiv \frac{Q_{\text{ext,ran}}(\text{shape}, a_{\text{eff}}, \lambda)}{Q_{\text{ext,ran}}(5:7:7 \text{ spheroid}, a_{\text{eff}}, \lambda)} \quad (\text{C4})$$

The ‘‘oblate’’ dielectric function used for the flattened shapes was derived by requiring that randomly-oriented 5:7:7 oblate spheroids reproduce the observed FIR opacity of dust in the diffuse ISM, while the ‘‘prolate’’ dielectric function used for the elongated shapes was derived by requiring that randomly-oriented 2:1:1 spheroids reproduce the observed opacity. Thus it is unsurprising that Figure 19a has  $R = 1$  for 5:7:7 spheroids, and 19b has  $R = 1$  for 2:1:1 spheroids. However, for other shapes,  $R_{\text{ext,ran}}(\lambda)$  remains of order unity, with  $0.85 \leq R_{\text{ext,ran}} < 1.6$  at  $\lambda > 10\mu\text{m}$  for all shapes

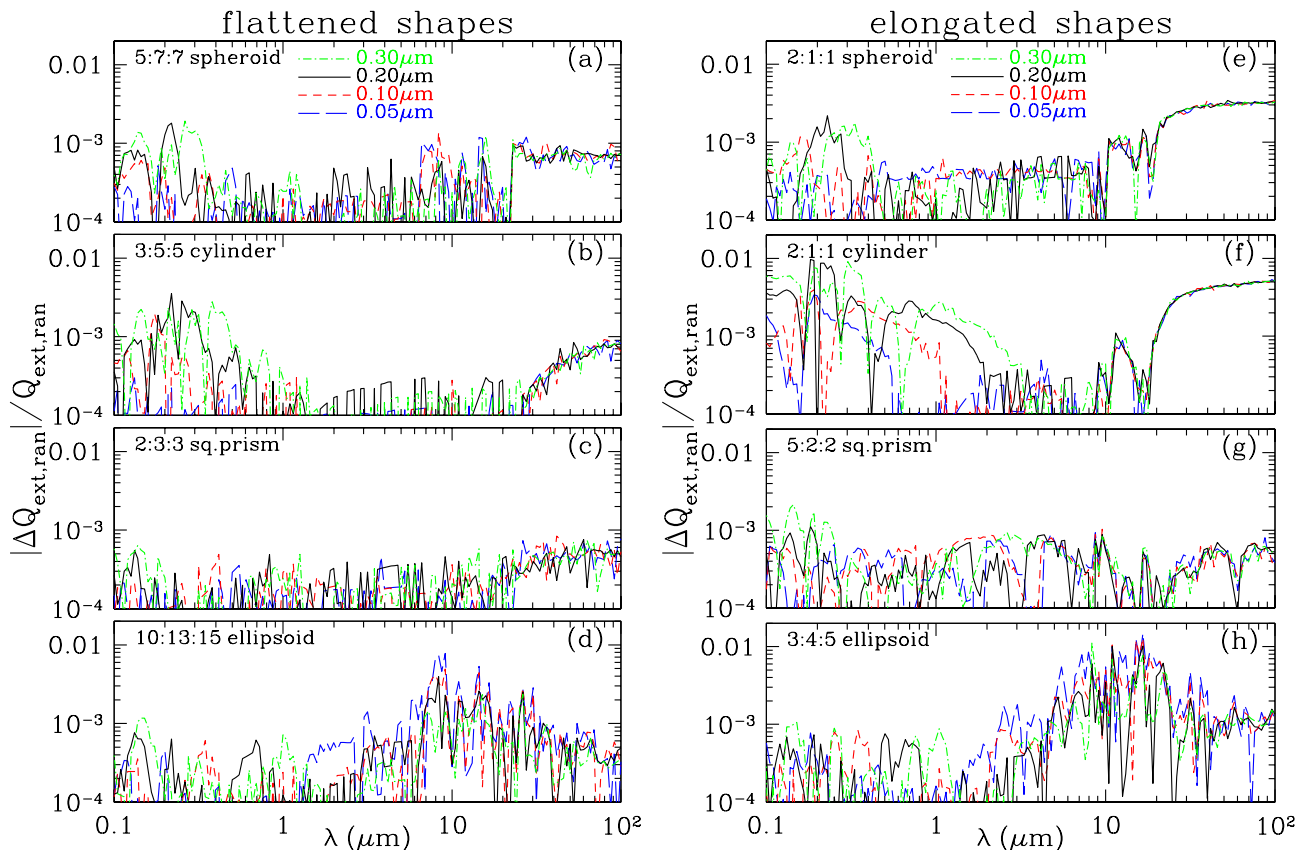


**Figure 17.** Fractional errors  $|\Delta Q_{\text{ext,ran}}|/Q_{\text{ext,ran}}$  as a function of wavelength  $\lambda$  for the shapes in Figure 6, for  $a_{\text{eff}} = 0.05, 0.10, 0.20, 0.30 \mu\text{m}$  and dielectric functions from Figure 2.  $Q_{\text{ext,ran}}$  is extrapolated using Equation (8), and  $\Delta Q_{\text{ext,ran}}$  is obtained from Equation (9) with the values of  $N$  given in Table 3.

shown. The largest values of  $R$  occur at the longest wavelengths, where  $\epsilon_1$  is large (see Figure 2) and the electric field within the grains depends on the grain shape. The sharp edges and corners present in cylinders and square prisms lead to enhanced absorption relative to spheroids in the FIR.

#### D. ORIENTATIONAL AVERAGING

For polarization cross sections, we assume perfect spinning alignment (PSA): the grain is spinning around the principal axis of largest moment of inertia  $\hat{\mathbf{a}}_1$ , with  $\hat{\mathbf{a}}_1 \parallel \mathbf{B}_0$ . We consider the case where the radiation is propagating in the  $\hat{\mathbf{z}}$  direction, and  $\mathbf{B}_0 \parallel \hat{\mathbf{x}}$  (i.e.,  $\mathbf{B}_0$  in the “plane of the sky”) (see Fig. 3).

Suppose the grain has a symmetry axis  $\hat{\mathbf{a}}$ . Let  $\hat{\mathbf{a}}_2 \perp \hat{\mathbf{a}}$  be a second axis fixed in the grain square prism, let  $\hat{\mathbf{a}}_2$  be normal to one of the sides). Let  $\beta$  measure target rotations around  $\hat{\mathbf{a}}$ , with  $\beta = 0$  when  $\hat{\mathbf{a}}_2$  is in the  $\hat{\mathbf{a}} - \hat{\mathbf{k}}$  plane. Let  $\Theta$  be the angle between  $\hat{\mathbf{a}}$  and the direction of propagation  $\hat{\mathbf{k}}$ .  $N$ -fold rotational symmetry implies

$$C(\Theta, \beta + 2\pi/N) = C(\Theta, \beta) \quad (\text{D5})$$

(e.g.,  $N = 1$  for a general asymmetric grain,  $N = 4$  for a square prism).

We require cross sections over  $\beta_{\text{min}} < \beta < \beta_{\text{max}}$  and  $0 < \Theta < \Theta_{\text{max}}$ . Set  $\beta_{\text{max}} = \pi/N$ . If the grain is symmetric under reflection through the  $\hat{\mathbf{a}}_1 - \hat{\mathbf{a}}_2$  plane<sup>9</sup> (e.g., the square prism), then  $\beta_{\text{min}} = 0$ ;

<sup>9</sup> I.e.,  $C(\Theta, \beta) = C(\Theta, -\beta)$ .

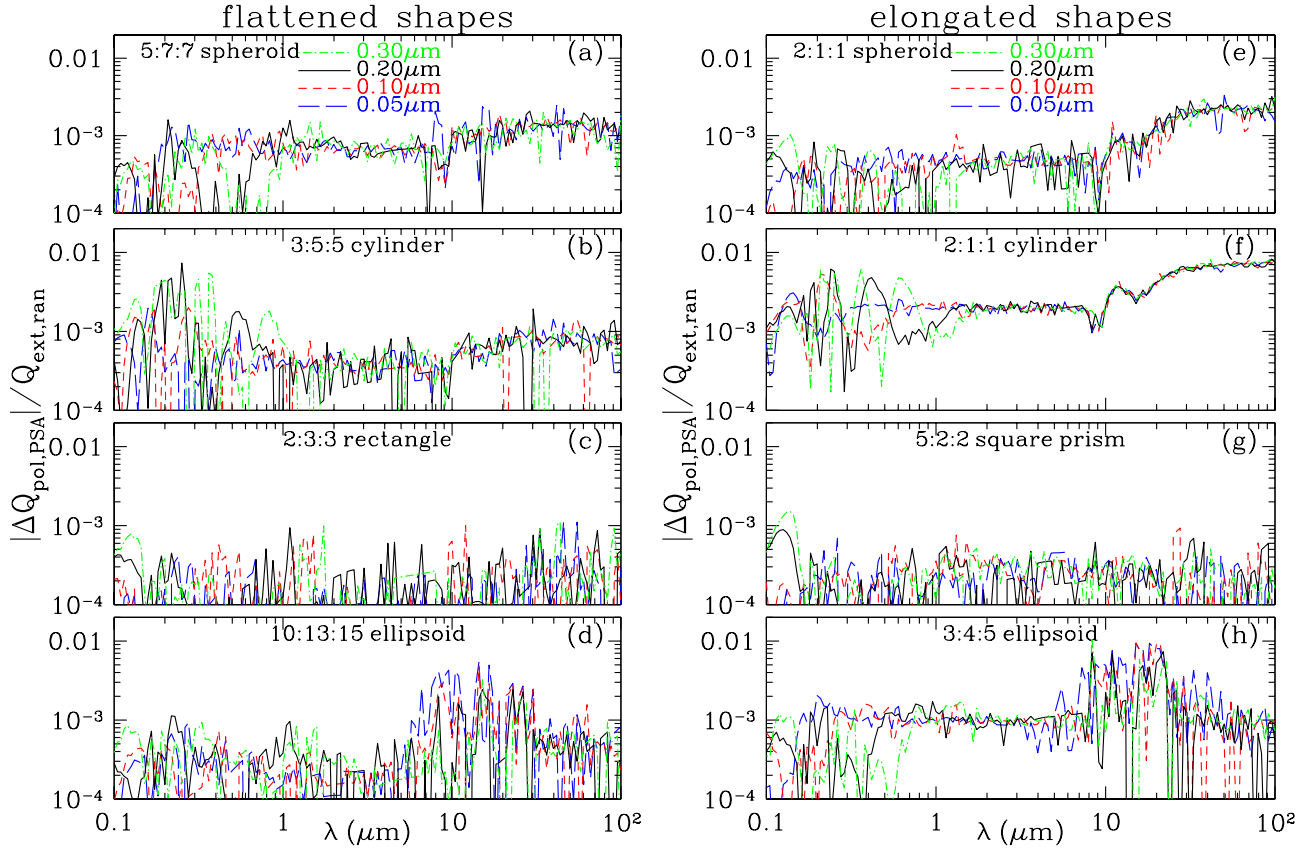


**Figure 18.**  $|\Delta Q_{\text{pol,PSA}}|/Q_{\text{ext,ran}}$  as a function of wavelength  $\lambda$  for the shapes in Figure 6, for  $a_{\text{eff}} = 0.05, 0.10, 0.20, 0.30 \mu\text{m}$  and dielectric functions from Figure 2.  $Q_{\text{pol,PSA}}$  is extrapolated using Equation (8), and  $\Delta Q_{\text{pol,PSA}}$  is obtained from Equation (9) with the values of  $N$  given in Table 3. [btd note: OMIT THIS?]

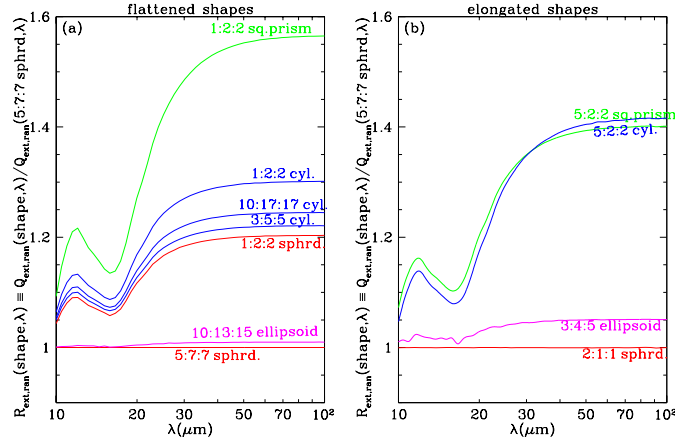


**Figure 19.** Wavelength dependence of the ratio  $R_{\text{ext,ran}}$  of the infrared opacity, relative to the opacity of 5:7:7 oblate spheroids (see Equation C4), for grain shapes with  $\Phi_{\text{PSA}} > 0.7$  and  $\sigma_p < 0.6$ . Cross sections were calculated using the “oblate” dielectric function  $\epsilon(\lambda)$  from Figure 2 for flattened shapes (left panel) and the “prolate”  $\epsilon(\lambda)$  for elongated shapes (right panel). All allowed shapes have  $1 \leq R_{\text{ext,ran}}(\lambda) \lesssim 1.6$  at  $\lambda > 10 \mu\text{m}$ . The largest values of  $R_{\text{ext,ran}}$  are for the square prisms and cylinders; sharp edges and corners evidently enhance the FIR absorption relative to the smooth spheroids.



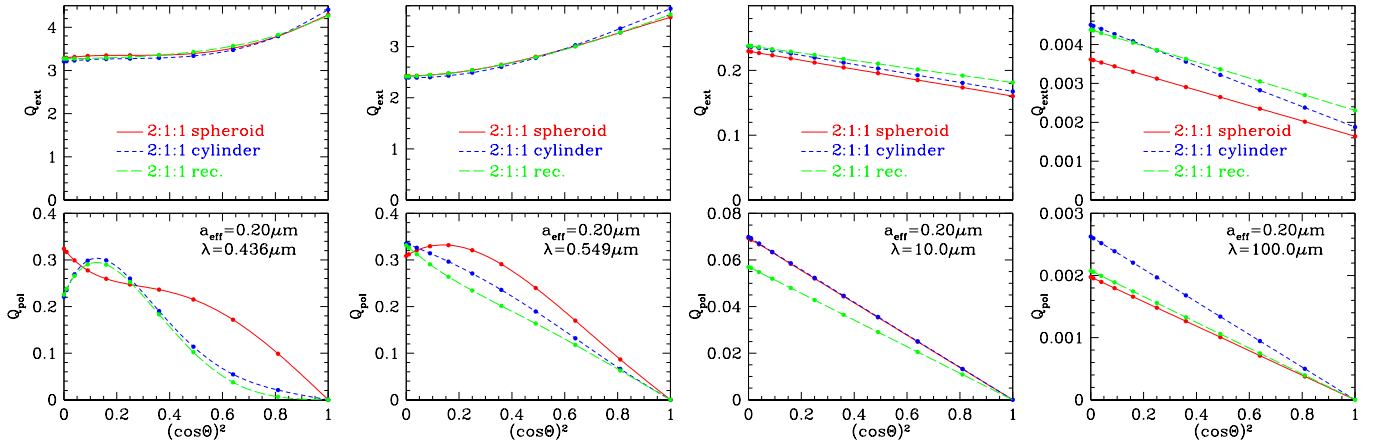


**Figure 20.** Dependence of  $Q_{\text{ext}}(\Theta)$  and  $Q_{\text{pol}}(\Theta)$  on orientation angle  $\Theta$  for four wavelengths  $\lambda$  and three axisymmetric shapes, with size  $a_{\text{eff}} = 0.2\mu\text{m}$ . For  $\lambda \gg a_{\text{eff}}$  (panels c and d), the grain is in the Rayleigh limit, with  $Q_{\text{ext}}$  and  $Q_{\text{pol}}$  both linear in  $\cos^2 \Theta$ . For  $\lambda$  comparable to  $a_{\text{eff}}$ , the dependence on  $\Theta$  becomes more complicated. For axially-symmetric shapes,  $Q_{\text{pol}} = 0$  for  $\cos^2 \Theta = 1$ .

otherwise  $\beta_{\text{min}} = -\pi/N$ . If the grain has reflection symmetry through a plane perpendicular to  $\hat{\mathbf{a}}$ ,<sup>10</sup> then  $\Theta_{\text{max}} = \pi/2$ ; otherwise  $\Theta_{\text{max}} = \pi$ .

Randomly-oriented grains have

$$Q_{\text{ext,ran}} = \frac{1}{\pi a_{\text{eff}}^2} \int_{\beta_{\text{min}}}^{\beta_{\text{max}}} \frac{d\beta}{[\beta_{\text{max}} - \beta_{\text{min}}]} \int_0^{\Theta_{\text{max}}} \frac{Q_{\text{ext}}(\Theta, \beta) \sin \Theta d\Theta}{1 - \cos(\Theta_{\text{max}})} \quad (\text{D6})$$

If the grain is spinning around axis  $\hat{\mathbf{a}}$  (e.g., flattened square prism) then

$$Q_{\text{pol,PSA}} = \frac{1}{2\pi a_{\text{eff}}^2} \int_{\beta_{\text{min}}}^{\beta_{\text{max}}} \frac{[C_{\text{ext,E}}(\Theta = \frac{\pi}{2}, \beta) - C_{\text{ext,H}}(\Theta = \frac{\pi}{2}, \beta)] d\beta}{(\beta_{\text{max}} - \beta_{\text{min}})} \quad (\text{D7})$$

If the grain is spinning around an axis  $\hat{\mathbf{a}}_1 \perp \hat{\mathbf{a}}$  (e.g., elongated square prism) then

$$Q_{\text{pol,PSA}} = \frac{1}{2\pi a_{\text{eff}}^2} \int_{\beta_{\text{min}}}^{\beta_{\text{max}}} \frac{d\beta}{(\beta_{\text{max}} - \beta_{\text{min}})} \int_0^{\Theta_{\text{max}}} [C_{\text{ext,E}}(\Theta, \beta) - C_{\text{ext,H}}(\Theta, \beta)] \frac{d\Theta}{\Theta_{\text{max}}} \quad (\text{D8})$$

<sup>10</sup> I.e.,  $C(\Theta, \beta) = C(\pi - \Theta, \beta)$ .